

# Convection-Permitting Simulations of Precipitation over the Peruvian Central Andes: Strong Sensitivity to Planetary Boundary Layer Parameterization

YONGJIE HUANG<sup>a</sup>, MING XUE<sup>a,b</sup>, XIAO-MING HU<sup>a,b</sup>, ELINOR MARTIN<sup>b,c</sup>, HECTOR MAYOL NOVOA<sup>d</sup>, RENEE A. MCPHERSON<sup>c,e</sup>, ANDRES PEREZ<sup>d</sup>, AND ISAAC YANQUI MORALES<sup>d</sup>

<sup>a</sup> Center for Analysis and Prediction of Storms, University of Oklahoma, Norman, Oklahoma

<sup>b</sup> School of Meteorology, University of Oklahoma, Norman, Oklahoma

<sup>c</sup> South Central Climate Adaptation Science Center, University of Oklahoma, Norman, Oklahoma

<sup>d</sup> Universidad Nacional de San Agustín de Arequipa, Arequipa, Perú

<sup>e</sup> Department of Geography and Environmental Sustainability, University of Oklahoma, Norman, Oklahoma

(Manuscript received 26 September 2022, in final form 12 May 2023, accepted 10 August 2023)

**ABSTRACT:** Regional climate dynamical downscaling at convection-permitting resolutions is now practical and has the potential to significantly improve over coarser-resolution simulations, but the former is not necessarily free of systematic biases. The evaluation and optimization of model configurations are therefore important. Twelve simulations at a grid spacing of 3 km using the WRF Model with different microphysics, planetary boundary layer (PBL), and land surface model (LSM) schemes are performed over the Peruvian central Andes during the austral summer, a region with particularly complex terrain. The simulated precipitation is evaluated using rain gauge data and three gridded precipitation datasets. All simulations correctly capture four precipitation hotspots associated with prevailing winds and terrain features along the east slope of the Andes, though they generally overestimate the precipitation intensity. The simulation using Thompson microphysics, Asymmetric Convection Model version 2 (ACM2) PBL, and Noah LSM schemes has the smallest bias. The simulated precipitation is most sensitive to PBL, followed by microphysics, and least sensitive to LSM schemes. The simulated precipitation is generally stronger in simulations using the YSU rather than the MYNN and ACM2 schemes. All simulations successfully capture the diurnal precipitation peak time mainly in the afternoon over the Peruvian central Andes and in the early morning along the east slope. However, there are significant differences over the western Amazon basin, where the precipitation peak occurs primarily in the late afternoon. Simulations using YSU exhibit a 4–8-h delay in the precipitation peak over the western Amazon basin, consistent with their stronger and more persistent low-level jets. These results provide guidance on the optimal configuration of a dynamical downscaling of global climate projections for the Peruvian central Andes.

**KEYWORDS:** South America; Precipitation; Model evaluation/performance; Parameterization

## 1. Introduction

Due to constraints of computing resources, state-of-the-art global climate models (GCMs) are still run at coarse grid spacings (50–100 km at most) (Juckes et al. 2020). Such resolutions are too coarse to resolve local-scale forcing and weather. The parameterized precipitation simulation in GCMs is generally poor (Giorgi 2019). Regional climate model (RCM) simulations nested with GCMs or regional climate dynamical downscaling have become an important tool to bring GCM resolutions to higher spatiotemporal resolutions and provide much more detail on local flows and climate (e.g., Giorgi and Bates 1989; Leung et al. 2003; Giorgi 2006; Solman 2013; Rummukainen et al. 2015; Sun et al. 2016; Hu et al. 2018; Ambrozzi et al. 2019; Giorgi 2019; Kendon et al. 2021). Higher-resolution RCMs improve the representation of lower boundary forcing, including those of complex topography, land use and land cover, coastlines, and mesoscale dynamical processes. Therefore, high-resolution RCMs are even more important for climate studies over regions with

particularly complex terrain, such as regions over the Andes in South America.

Many previous studies have indicated the added value of higher-resolution RCMs over different climate zones, compared to GCMs, lower-resolution RCMs, or even low-resolution reanalyses (e.g., Feser et al. 2011; Solman 2013; Torma et al. 2015; Rummukainen 2016; Giorgi 2019; Ciarlo et al. 2020). For example, Kanamitsu and Kanamaru (2007) showed the advantage of a 10-km simulation in near-surface wind and temperature over California from diurnal cycle to multidecadal trend compared to the NCEP–NCAR reanalysis at a grid spacing of ~200 km. Gao et al. (2006) demonstrated improvement in the simulation of East Asian precipitation when decreasing horizontal grid spacing from 360 to 45 km. Torma et al. (2015) found a substantial added value of RCMs at horizontal resolutions of 0.44° (~50 km) and 0.11° (~12 km) for different metrics of precipitation over the European Alps areas characterized by complex terrain compared to the driving GCMs. Moufouma-Okia and Jones (2015) showed improvements with increasing horizontal resolutions with grid spacings from 150 to 12 km in rainfall simulation over Africa. Lucas-Picher et al. (2017) highlighted the added value of finer resolutions in the simulations of five North American weather phenomena, including orographic precipitation and snow in the Rocky Mountains, the North

Corresponding author: Ming Xue, mxue@ou.edu

DOI: 10.1175/JHM-D-22-0173.1

© 2023 American Meteorological Society. This published article is licensed under the terms of the default AMS reuse license. For information regarding reuse of this content and general copyright information, consult the AMS Copyright Policy ([www.ametsoc.org/PUBSReuseLicenses](http://www.ametsoc.org/PUBSReuseLicenses)).

Brought to you by UNIVERSITY OF OKLAHOMA LIBRARY | Unauthenticated | Downloaded 10/17/23 08:09 PM UTC

American monsoon, snowbelts around the Great Lakes, wind in the Saint Lawrence River valley, and the diurnal cycle of precipitation over Florida and the Caribbean. Falco et al. (2020) confirmed the added value of RCMs in simulating extreme precipitation and mean surface temperature in South America by six RCM simulations at a resolution of  $\sim 50$  km from the World Climate Research Programme (WCRP) Coordinated Regional Downscaling Experiment (CORDEX; Gutowski et al. 2016).

All aforementioned studies ran RCMs at grid spacings of tens of kilometers, in which deep convection cannot be resolved explicitly and has to be parameterized. The parameterization of convection is considered a major source of uncertainty and has significant biases in RCM simulations of precipitation (Prein et al. 2015, 2020; Giorgi 2019; Lucas-Picher et al. 2021). In convection-permitting models (CPMs) with horizontal grid spacings of a few kilometers (generally  $< 4$  km), convection parameterization can be switched off, and deep convection can develop explicitly. Many studies have shown substantial improvements in precipitation simulation of CPMs compared to convection-parameterized models in different regions around the world, including Europe (e.g., Prein et al. 2013; Fosser et al. 2015; Berthou et al. 2020; Fumière et al. 2020; Lind et al. 2020), North America (e.g., Sun et al. 2016; Gao et al. 2017), Asia (e.g., Karki et al. 2017; Zhu et al. 2018; Li et al. 2021), and Africa (e.g., Kouadio et al. 2020). Fosser et al. (2015) showed the performance of an hourly intensity distribution and diurnal cycle of precipitation in southwestern Germany is significantly improved in the 2.8-km RCM simulations compared to the 50- and 7-km RCM simulations. Sun et al. (2016) showed that the 4-km convection-permitting simulation of summer precipitation over the Great Plains in the United States outperforms the simulation at a 25-km grid spacing in the extreme precipitation magnitude and precipitation diurnal cycle, benefiting from the more realistic simulations of the low-level jet and related atmospheric circulations in the 4-km run. Gao et al. (2017) examined simulations of summer precipitation over the conterminous United States at grid spacings of 36, 12, and 4 km and also found the 4-km convection-permitting simulations most skillfully reproduced the spatial distributions and diurnal cycle of the observed precipitation. Zhu et al. (2018) showed that forecasts at a 4-km grid spacing over China during the summer season outperformed global model forecasts in terms of spatial distribution, intensity, and diurnal variation of precipitation. These improvements of CPMs in precipitation simulation can be attributed to better-resolved land surface conditions, explicit representation of convection, and more realistic representation of local- and mesoscale dynamics (Prein et al. 2013; Sun et al. 2016; Zhu et al. 2018). For these reasons, convection-permitting RCM simulations have been increasingly used whenever computational resources allow (e.g., Prein et al. 2015; Liu et al. 2017; Stratton et al. 2018; Fendon et al. 2019; Chan et al. 2020; Coppola et al. 2020; Fosser et al. 2020; Guo et al. 2020; Lind et al. 2020; Prein et al. 2020).

Weather and climate in South America are strongly influenced by the complex Andes topography and synoptic

features such as the South American low-level jet (SALLJ; Marengo et al. 2002; Vernekar et al. 2003; Vera et al. 2006; Salio et al. 2007; Romatschke and Houze 2010; Mohr et al. 2014; Rasmussen and Houze 2016; Jones 2019; Montini et al. 2019; Chavez et al. 2020; Poveda et al. 2020). The rising and withdrawing of the nocturnal SALLJ with high instability and abundant moisture trigger the extreme austral summer convection on the east slope and foothills of the central Andes, respectively (Romatschke and Houze 2010; Chavez et al. 2020). To date, there have been numerous RCM simulations conducted in South America (e.g., Roads et al. 2003; Vernekar et al. 2003; Marengo et al. 2010; Solman 2013; Gutowski et al. 2016; Ambrizzi et al. 2019; Martinez et al. 2019; Solman and Blázquez 2019; Zaninelli et al. 2019; Avila-Diaz et al. 2020; Falco et al. 2020; Chimborazo and Vuille 2021; Hodnebrog et al. 2022; Martinez et al. 2022; da Silva et al. 2023). However, almost all these RCM simulations were performed at grid spacing of tens of kilometers, and few convection-permitting RCM simulations have been conducted over South America (e.g., Schumacher et al. 2020; Bettolli et al. 2021; Lavin-Gullon et al. 2021; Junquas et al. 2022). Bettolli et al. (2021) examined four convection-permitting RCM simulations and four statistical downscaling models in simulating daily extreme precipitation events in southeastern South America in the warm season from October 2009 to March 2010 and found that most models are able to capture the selected extreme events, despite a large spread in accumulated values and the location of heavy precipitation among the models, which was also indicated by Lavin-Gullon et al. (2021). Hodnebrog et al. (2022) downscaled three GCMs to 50-km horizontal grid spacing over South America and to 10-km grid spacing for central Chile, Peru, and southern Brazil and found that increasing the model resolution could produce a different sign for precipitation trend projections for Peru and southern Brazil. They suggested that an ensemble of CPM simulations is necessary to increase the reliability of precipitation projection for Peru and southern Brazil, where convective precipitation is dominant. Schumacher et al. (2020) found that a 3-km simulation achieves a better performance of precipitation as elevation increases, most likely due to the better-resolved topography in the central Andes of Chile and Argentina. Some short-period modeling studies (e.g., Mourre et al. 2016; Moya-Álvarez et al. 2019; Paccini and Stevens 2023) also emphasized the added value of convection-permitting resolutions in improving precipitation simulations across various regions in Peru and over the Amazon basin. Supported by funding from Universidad Nacional de San Agustín de Arequipa, Arequipa, Peru, this project seeks to perform future climate projections for Peru and the surrounding regions at a 3-km grid spacing based on the Weather Research and Forecasting (WRF) Model (Skamarock et al. 2019) to examine projected changes in high-impact weather events in the Peruvian central Andes region (Poveda et al. 2020). Before actually conducting future climate simulations over decadelong periods, we want to evaluate and optimize the configurations of the model for the region.

Convection-permitting simulations of precipitation are strongly influenced by physics parameterizations, including microphysics (MP), planetary boundary layer (PBL), and

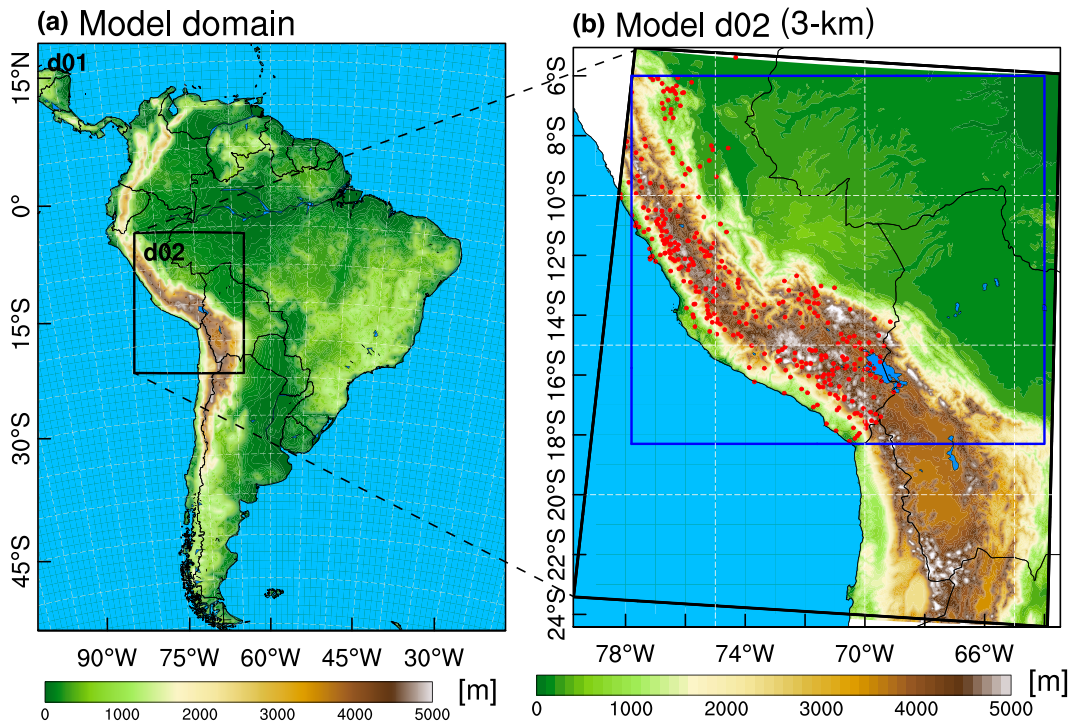


FIG. 1. (a) The model domain configuration (color-shaded fields represent terrain elevation; m). (b) Terrain elevation in the 3-km domain with rain gauge locations marked by red dots. The blue rectangle indicates the study area in this study.

land surface model (LSM) schemes (e.g., [Zhu and Xue 2016](#); [Feng et al. 2018](#); [Guo et al. 2019](#); [He et al. 2019](#); [Huang et al. 2020](#); [Kouadio et al. 2020](#); [Taraphdar et al. 2021](#); [González-Rojí et al. 2022](#)). [González-Rojí et al. \(2022\)](#) examined the sensitivity of precipitation over southern Peru to physics parameterization schemes in WRF, version 3.8.1; however, very limited physics schemes and combinations were tested in their study. As the first step to conduct a long-term convection-permitting regional climate simulation, a series of 2-month convection-permitting simulations using different physics parameterization schemes are performed over the Peruvian central Andes during the austral summer using the planned nested grid configuration. It should be noted that initially a configuration using Thompson MP, Yonsei University (YSU) PBL, and Noah LSM schemes based on previous studies was used to make a 10-yr simulation over 2010–19. It was found that precipitation was significantly overpredicted ([Chen et al. 2022](#)), which also motivated this study to compare configurations using combinations of different MP, PBL, and LSM schemes. The main objective of this study is to evaluate the performance of WRF-based CPMs in simulating precipitation over the Peruvian central Andes by comparing them with available best observational data. The results of this study will provide guidance on the optimal configuration of CPMs for future climate dynamical downscaling for the Peruvian central Andes region.

The rest of this paper is organized as follows. [Section 2](#) describes the model and experiment setup and observational data used for evaluation. [Section 3](#) presents and discusses the

precipitation evaluation results. A summary is presented in [section 4](#).

## 2. Method and data

### a. Model setup

The WRF Model, version 4.2.1 ([Skamarock et al. 2019](#)), is used. Hourly data from the fifth major global reanalysis produced by the European Centre for Medium-Range Weather Forecasts (ERA5); ([Hersbach et al. 2020](#)) are used for initial and boundary conditions for the simulations. Two one-way nested domains at 15- and 3-km horizontal grid spacings are used, which cover the entire South American and Peruvian central Andes regions, respectively ([Fig. 1a](#)). Both domains use 61 stretched vertical levels topped at 20 hPa. A spectral nudging technique ([Miguez-Macho et al. 2004](#)) is applied to the outer 15-km domain to maintain large-scale circulations. The spectral nudging configurations are similar to those in [Hu et al. \(2018\)](#). The nudging variables include horizontal wind components, temperature, moisture, and geopotential height above PBL height. Nudging wavenumbers of 5 and 3 in the zonal and meridional directions, respectively, and a nudging coefficient of  $3 \times 10^{-5} \text{ s}^{-1}$  are adopted throughout the simulation period. The simulations cover 2 months (January and February 2019) during the austral summer, with the first month treated as the spinup period mainly for land surface models. Limited by computational resources, the simulations cannot span multiple years. Based on the assumption that the

TABLE 1. Physics parameterization schemes in the 12 sensitivity experiments.

Experiment	MP	PBL	LSM
THOM_YSU_Noah	THOM	YSU	Noah
THOM_YSU_NoahMP	THOM	YSU	NoahMP
THOM_YSU_CLM	THOM	YSU	CLM
THOM_MYNN_Noah	THOM	MYNN	Noah
THOM_MYNN_NoahMP	THOM	MYNN	NoahMP
THOM_ACM2_Noah	THOM	ACM2	Noah
THOM_ACM2_NoahMP	THOM	ACM2	NoahMP
THOMA_YSU_Noah	THOMA	YSU	Noah
WSM6_YSU_Noah	WSM6	YSU	Noah
WSM6_MYNN_Noah	WSM6	MYNN	Noah
MORR_YSU_Noah	MORR	YSU	Noah
MORR_MYNN_Noah	MORR	MYNN	Noah

relative performance for precipitation can be revealed by simulations over a couple of months in the rainy season, we choose to run over 2 months from January to February, which are the climatological peak months of precipitation during the austral summer (Mohr et al. 2014; Espinoza et al. 2015).

The combinations of MP, PBL, and LSM schemes of the 12 sensitivity experiments examined in this study are listed in Table 1. The MP schemes include the Thompson scheme (THOM; Thompson et al. 2008), Thompson aerosol-aware scheme (THOMA; Thompson and Eidhammer 2014), WRF single-moment 6-class (WSM6) scheme (Hong and Lim 2006), and Morrison 2-moment scheme (MORR; Morrison et al. 2009). The PBL schemes include the YSU scheme (Hong and Lim 2006), Mellor–Yamada–Nakanishi–Niino (MYNN) level 2.5 scheme (Nakanishi and Niino 2009), and Asymmetric Convection Model version 2 (ACM2) scheme (Pleim 2007). The LSM schemes include the unified Noah LSM (Noah; Ek et al. 2003), Noah multiple-physics LSM (NoahMP; Niu et al. 2011), and Community Land Model (CLM) version 4 (Lawrence et al. 2011). Other physics parameterizations are the same among the sensitivity experiments, including the revised MM5 Monin–Obukhov surface layer scheme (Jiménez et al. 2012) and the Rapid Radiative Transfer Model for GCMs (RRTMG) longwave and shortwave radiation schemes (Iacono et al. 2008). The Tiedtke cumulus parameterization scheme (Tiedtke 1989) is used only for the 15-km domain.

### b. Observational data

Three gridded global precipitation datasets, including half-hourly Integrated Multi-satellite Retrievals for GPM (IMERG) at a horizontal resolution of  $0.1^\circ \times 0.1^\circ$  (Huffman et al. 2019), half-hourly NOAA Climate Prediction Center (CPC) morphing technique (CMORPH) global precipitation analyses at a horizontal grid spacing of  $\sim 8$  km (Joyce et al. 2004), and 3-hourly Multi-Source Weighted-Ensemble Precipitation (MSWEP) version 2 at a horizontal resolution of  $0.1^\circ \times 0.1^\circ$  (Beck et al. 2019), are used for the evaluation of simulated monthly and diurnal precipitation. IMERG incorporates a monthly gauge analysis product produced by the Global Precipitation Climatology Centre (GPCC) at a grid

spacing of  $1^\circ$  (Huffman et al. 2019), and MSWEP uses daily observations from gauges worldwide to determine the merging weights, calculate the wet-day biases for the reanalyses, and correct the precipitation estimates near gauge stations (Beck et al. 2019). However, gauge stations used by IMERG and MSWEP are very sparse in our study region (Huffman et al. 2019; Beck et al. 2019). CMORPH does not blend rainfall station gauge data into its estimates (Joyce et al. 2004). The monthly precipitation data of about 400 rain gauge stations in Peru (Fig. 1b) (Aybar et al. 2020) are also used for the evaluation of global precipitation datasets and simulated precipitation. Due to the limited spatial coverage and coarse temporal resolutions of rain gauge data, evaluations of the spatial distribution and diurnal cycle of precipitation are mainly based on the global precipitation datasets.

For the comparison among the precipitation datasets at different resolutions, CMORPH, MSWEP, and the simulated precipitation fields are regridded to the IMERG grid ( $0.1^\circ \times 0.1^\circ$ ) by using the “patch recovery” technique (Sun et al. 2016).

### c. Evaluation metrics

The mean bias (MB) is used to examine the mean error, given by

$$\text{MB} = \frac{1}{N} \sum_{i=1}^N (M_i - O_i), \quad (1)$$

where  $N$  is the total number of samples and  $M$  and  $O$  represent simulations and observations, respectively.

The root-mean-square error (RMSE) is selected to examine the average magnitude of the simulation errors, which is

$$\text{RMSE} = \sqrt{\frac{1}{N} \sum_{i=1}^N (M_i - O_i)^2}. \quad (2)$$

To characterize the variation/shape of the distribution for a given variable, the Taylor skill score (TSS) (Taylor 2001) is adopted and given by

$$\text{TSS} = \frac{4(1 + R)}{\left[ \left( \sigma_r + \frac{1}{\sigma_r} \right)^2 (1 + R_0) \right]}, \quad (3)$$

where  $\sigma_r$  is the normalized standard deviation given by simulated root-mean-square (RMS) divided by the observed RMS,  $R$  is the correlation coefficient, and  $R_0$  is the maximum correlation attainable, which is set to 1. Thus, if the correlation coefficient and normalized standard deviation are 1, TSS is 1.

## 3. Results

### a. Monthly precipitation

The mean daily precipitation of the three precipitation products and simulations in February 2019 is shown in Fig. 2 to examine the spatial distribution characteristics. Similar

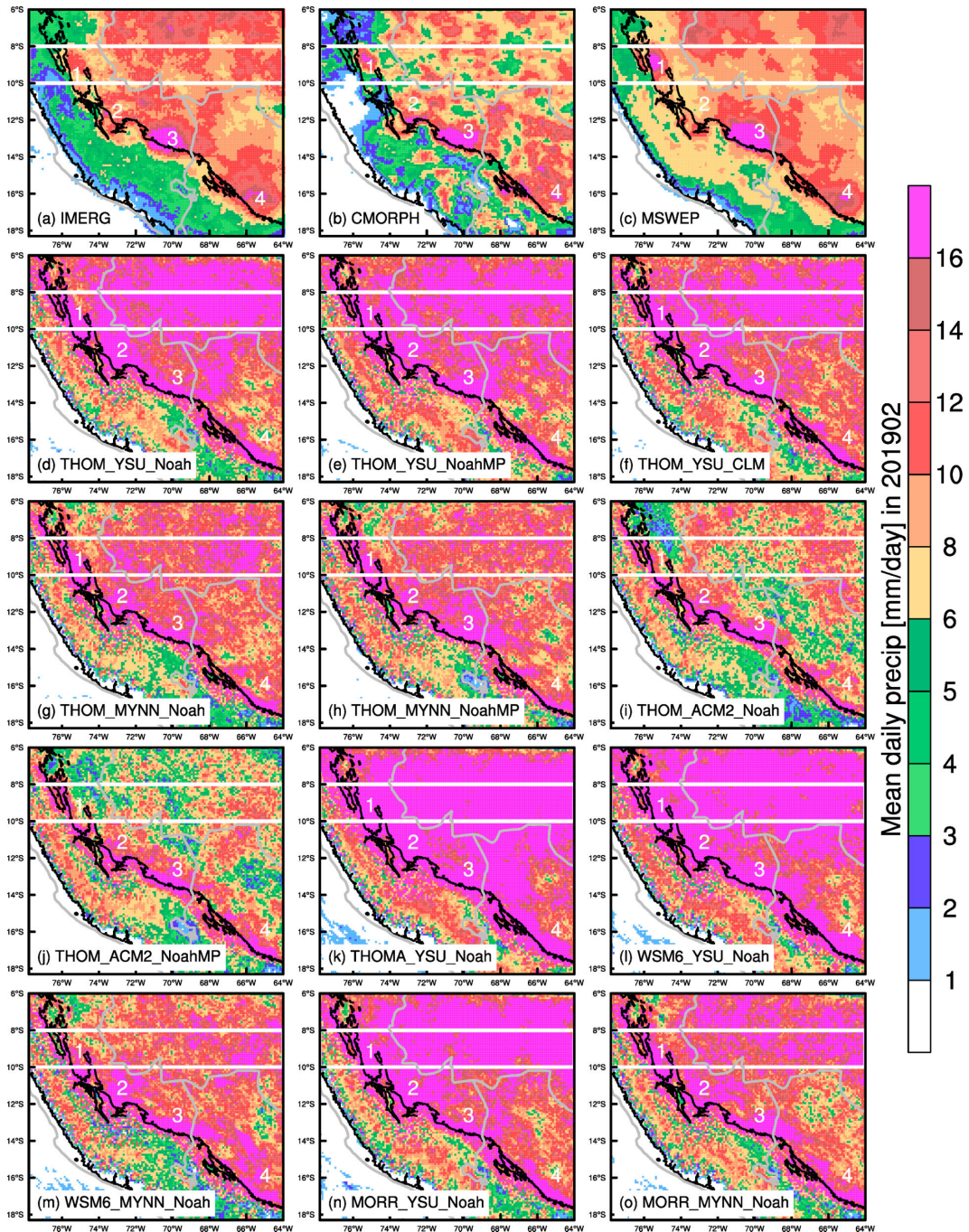


FIG. 2. Monthly precipitation (shaded;  $\text{mm day}^{-1}$ ) of (a)–(c) precipitation products and (d)–(o) WRF simulations using different physics schemes in February 2019. The black contour in each panel represents 1-km terrain elevation. The white rectangle in each panel indicates the region for the Hovmöller diagram in Fig. 7.

results were found in January 2019, although this is treated as the spinup period. Thus, results in February 2019 are discussed in detail here. There are four precipitation hotspots along the east slope of the Peruvian central Andes (marked by numbers in white in Fig. 2), although there exists a difference in precipitation intensity among the three precipitation products (Figs. 2a–c). The four hotspots are all near the

notches of terrain, indicating that terrain plays an important role in producing these hotspots, which was also indicated in previous studies (e.g., Mohr et al. 2014; Espinoza et al. 2015; Chavez and Takahashi 2017; Junquas et al. 2018). Precipitation data from IMERG and MSWEP are closer to each other in terms of precipitation distribution and intensity over the western Amazon basin to the east of the Peruvian central

Andes (Figs. 2a,c). All simulations successfully capture the four precipitation hotspots. However, they overestimate their intensity compared to IMERG and MSWEP, with the maximum precipitation intensity being generally over  $16 \text{ mm day}^{-1}$  (Fig. 2). The mean daily precipitation over the entire western Amazon basin is larger than  $16 \text{ mm day}^{-1}$  in the simulations using the YSU PBL scheme combined with different MP and LSM schemes (Figs. 2d–f,k,l,n), while both those in IMERG and MSWEP are less than  $16 \text{ mm day}^{-1}$  in this region (Figs. 2a,c). This means that no matter what MP or LSM schemes are used, simulations using the YSU PBL scheme tend to produce larger mean daily precipitation. The MYNN PBL scheme (Figs. 2g,h,m,o) simulates a smaller area, and the ACM2 PBL scheme (Figs. 2d–f,k,l,n) simulates an even smaller area, with precipitation over  $16 \text{ mm day}^{-1}$  in the western Amazon basin. Therefore, among the MP, PBL, and LSM schemes tested in this study, WRF simulations of total precipitation are the most sensitive to the PBL scheme, followed by the MP scheme, and least sensitive to the LSM scheme (Figs. 2d–o). It should be noted that the findings regarding the sensitivity of WRF simulations of total precipitation are based on the schemes tested in this study, which may not cover all possible configurations.

In February 2019, compared to the rain gauge data (mean daily precipitation of  $\sim 5.25 \text{ mm day}^{-1}$ ), IMERG and CMORPH generally underestimate the mean daily precipitation, with mean biases of  $-1.70$  and  $-1.90 \text{ mm day}^{-1}$ , respectively (Figs. 3a,b), while MSWEP generally has a positive bias, with a mean bias of  $0.29 \text{ mm day}^{-1}$  (Fig. 3c). Among the three precipitation products (Figs. 3a–c), MSWEP has the smallest RMSE of  $2.08 \text{ mm day}^{-1}$ , while RMSEs in IMERG and CMORPH are  $2.87$  and  $3.80 \text{ mm day}^{-1}$  respectively. Thus, the precipitation of MSWEP is closer to rain gauge data than those of IMERG and CMORPH. All simulations generally overestimate precipitation (Figs. 3d–o), with the smallest mean bias of  $0.49 \text{ mm day}^{-1}$  and RMSE of  $2.85 \text{ mm day}^{-1}$  in THOM\_ACM2\_Noah (Fig. 3i) and the largest mean bias of  $3.92 \text{ mm day}^{-1}$  and RMSE of  $6.00 \text{ mm day}^{-1}$  in THOMA\_YSU\_Noah (Fig. 3k).

To quantify the differences, TSS as a function of the relative mean (simulated mean divided by referenced mean) and mean bias as a function of the RMSE of simulated mean daily precipitation in February 2019 relative to IMERG, CMORPH, and MSWEP, respectively (Fig. 4), are examined. The results based on IMERG and MSWEP are similar to each other, while they are more different from those based on CMORPH. As discussed above, IMERG and MSWEP are more reliable than CMORPH; therefore, our further discussions are mainly based on MSWEP. Among all simulations, THOM\_ACM2\_Noah has the highest TSS ( $\sim 0.76$ ), and its relative mean is close to 1 (Fig. 4a). Meanwhile, THOM\_ACM2\_Noah has the lowest RMSE ( $\sim 4.4 \text{ mm day}^{-1}$ ), and its mean bias is near 0 (Fig. 4b). Therefore, based on these metrics, THOM\_ACM2\_Noah is generally better than the other simulations. Changing the LSM to NoahMP, the TSS, bias, and RMSE in THOM\_ACM2\_NoahMP are changed slightly to  $\sim 0.73$ , approximately  $-0.25$ , and  $\sim 4.8 \text{ mm day}^{-1}$ , respectively (Fig. 4). However, changing the PBL scheme, the TSS, bias, and RMSE are changed significantly to  $\sim 0.55$ ,  $\sim 4.8$ , and  $\sim 8.0 \text{ mm day}^{-1}$ ,

respectively, in THOM\_YSU\_Noah and to  $\sim 0.68$ ,  $\sim 2.3$ , and  $\sim 5.6 \text{ mm day}^{-1}$ , respectively, in THOM\_MYNN\_Noah (Fig. 4). When changing the MP scheme, the ranges of TSS, bias, and RMSE are  $\sim 0.13$  ( $0.42$ – $0.55$ ),  $\sim 3.4$  ( $4.8$ – $8.2$ ), and  $\sim 3.5$  ( $8.0$ – $11.5$ )  $\text{mm day}^{-1}$ , respectively, among the simulations of THOM\_YSU\_Noah, THOMA\_YSU\_Noah, WSM6\_YSU\_Noah, and MORR\_YSU\_Noah. Their ranges are  $\sim 0.03$  ( $0.67$ – $0.70$ ),  $\sim 1.2$  ( $1.9$ – $3.1$ ), and  $\sim 0.7$  ( $5.3$ – $6.0$ )  $\text{mm day}^{-1}$ , respectively, among the simulations of THOM\_MYNN\_Noah, WSM6\_MYNN\_Noah, and MORR\_MYNN\_Noah. They are all smaller than the ranges of changing the PBL scheme, which are  $\sim 0.21$  ( $0.55$ – $0.76$ ),  $\sim 4.8$  ( $0.0$ – $4.8$ ), and  $\sim 3.6$  ( $4.4$ – $8.0$ )  $\text{mm day}^{-1}$ , respectively, among the simulations of THOM\_YSU\_Noah, THOM\_MYNN\_Noah, and THOM\_ACM2\_Noah. Therefore, based on these objective metrics, simulations are more sensitive to the PBL scheme among the schemes tested in this study, and the simulation of THOM\_ACM2\_Noah is the closest to precipitation products IMERG and MSWEP.

### b. Diurnal cycle of precipitation

Figure 5 shows the precipitation peak time calculated from the hourly precipitation of IMERG, CMORPH, and simulations using different physics schemes in February 2019. The average diurnal precipitation in the mountain, foothill, and plains regions are displayed in Fig. 6. Because MSWEP is 3-hourly average precipitation, and it cannot accurately depict the precipitation peak (Fig. 6), it is not included in Fig. 5. Although there are differences in precipitation intensity between IMERG and CMORPH (Figs. 2a,b), their precipitation peak times are very consistent with each other (Figs. 5a,b). Previous studies (e.g., Dezfouli et al. 2017; O and Kirstetter 2018; Tan et al. 2019; Watters and Battaglia 2019; de Sousa Afonso et al. 2020) have demonstrated that IMERG has the ability to accurately capture the diurnal cycle of precipitation in different regions, including South America. Over the Peruvian central Andes for terrain elevation higher than 1 km, the precipitation peak time is mainly in the afternoon during  $\sim 1400$ – $1900$  LST (Figs. 5a,b). The average precipitation peak in the mountain region is at about 1600 LST, with  $\sim 0.47$  and  $\sim 0.33 \text{ mm h}^{-1}$  in IMERG and CMORPH, respectively (Fig. 6a). Along the east slope of the Peruvian central Andes for terrain elevations less than 1 km, the precipitation peak time is mainly in the early morning ( $\sim 0000$ – $0600$  LST) (Figs. 5a,b, 6b). Over the western Amazon basin to the east of the Peruvian central Andes, the precipitation peak time is mainly during  $\sim 1100$ – $1700$  LST (Figs. 5a,b), with the maximum average precipitation of  $\sim 0.84$  and  $\sim 0.80 \text{ mm h}^{-1}$  in IMERG and CMORPH, respectively (Fig. 6c). The simulations successfully capture the precipitation peak time over the Peruvian central Andes and also along the east slope (Figs. 5c–n), with their precipitation peak times basically in the same time periods as those of IMERG and CMORPH. However, all simulations overestimate the precipitation intensity in these periods, with the simulations using the ACM2 PBL scheme being closer to IMERG (Figs. 6a,b). There exist larger differences in the simulated precipitation peak time over the western Amazon basin compared to the observed time (Fig. 5). In the

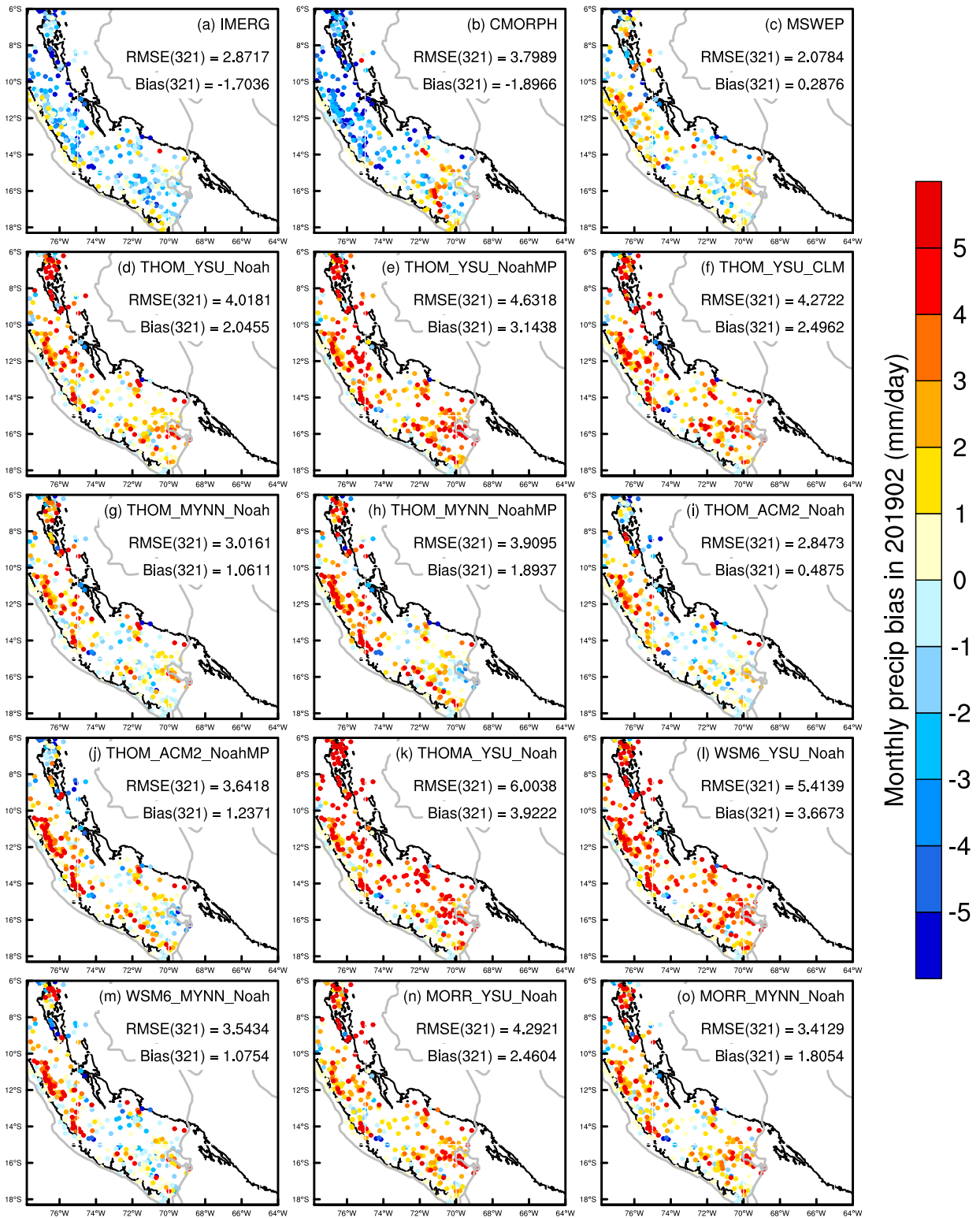


FIG. 3. Monthly precipitation biases [difference between (a)–(c) precipitation products or (d)–(o) WRF simulations in the 3-km domain using different physics schemes and the rain gauge data;  $\text{mm day}^{-1}$ ] in February 2019. The RMSE and MB along with the number of samples in parentheses are given in each panel. The black contour in each panel represents 1-km terrain elevation.

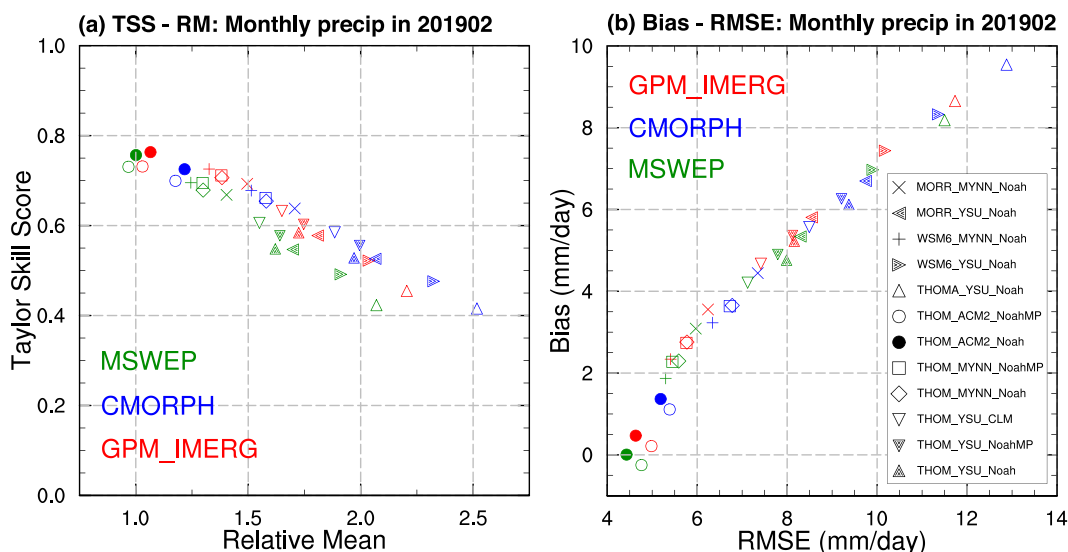


FIG. 4. Scatterplots of (a) TSS as a function of relative mean (simulated mean divided by referenced mean) and (b) bias ( $\text{mm day}^{-1}$ ) as a function of RMSE ( $\text{mm day}^{-1}$ ) of simulated monthly precipitation in February 2019 relative to IMERG (red), CMORPH (blue), and MSWEP (green), respectively.

simulations using the YSU PBL scheme (except MORR\_YSU\_Noah), the precipitation peak time in the region  $8^{\circ}$ – $11^{\circ}\text{S}$ ,  $67^{\circ}$ – $70^{\circ}\text{W}$  over the western Amazon basin is delayed by about 4–8 h compared to those of IMERG and CMORPH (Figs. 5a–e,j,k,m), and their averaged precipitation has two peaks at  $\sim 1300$  and  $\sim 0200$  LST (Fig. 6c). The precipitation at the latter peak can be reduced when using other PBL schemes, especially the ACM2 scheme (Fig. 6c); thus, the delay bias in the simulated precipitation peak time can also be reduced (Figs. 5f–i,l,n).

To examine the evolution of diurnal precipitation in the region with a larger bias over the western Amazon basin, Hovmöller diagrams of precipitation from IMERG, CMORPH, and simulations using different physics schemes in February 2019 are created and shown in Fig. 7. The precipitation evolutions between IMERG and CMORPH are very consistent with each other (Figs. 7a,b). Precipitation over the Andes for terrain elevations higher than 2 km ( $\sim 78^{\circ}$ – $76^{\circ}\text{W}$ ) mainly starts at  $\sim 1600$  UTC (1100 LST) and ends at  $\sim 0800$  UTC (0300 LST) the next day (Figs. 7a,b). At the east slope and foothills of the Andes for terrain elevations lower than 2 km ( $\sim 76^{\circ}$ – $74^{\circ}\text{W}$ ), precipitation has a peak between 0800 and 1200 UTC (0300 and 0700 LST) (Figs. 7a,b), which is consistent with that shown in Figs. 5a and 5b. Over the western Amazon basin ( $\sim 74^{\circ}$ – $66^{\circ}\text{W}$ ), precipitation is mainly during  $\sim 1500$ – $2400$  UTC (1000–1900 LST) and can be extended to 0800 UTC (0300 LST) the next day for the region between  $72^{\circ}$  and  $68^{\circ}\text{W}$ , with the peak at around 2100 UTC (1600 LST) (Figs. 7a,b). All simulations basically capture the main precipitation period over the Andes, at the east slope and foothills of the Andes, and over the western Amazon basin (Figs. 7c–n); however, the simulated precipitation intensities are overestimated, especially for the simulations using the YSU PBL scheme, with large areas of precipitation  $> 1.4 \text{ mm h}^{-1}$ . The precipitation

peak in the region between  $70^{\circ}$  and  $66^{\circ}\text{W}$  is mainly within 0000–1200 UTC (1900–0700 LST) in the simulations using the YSU PBL scheme, except for in MORR\_YSU\_Noah (Figs. 7c–e,j,k,m), where it is different from those of IMERG and CMORPH (Figs. 7a,b). This bias can be reduced in simulations using other PBL schemes, especially the ACM2 scheme (Figs. 7f–i,l,n). Generally, the precipitation evolution and intensity in THOM\_ACM2\_Noah are closer to those in IMERG than those in other simulations. These results are consistent with those shown in Figs. 2 and 5.

Overall, through the subjective and objective evaluations of monthly and diurnal precipitation, all simulations generally capture the main characteristics of observations, while they generally overestimate the precipitation amount, especially in complex terrain regions, which is similar to previous CPM studies in different regions, such as East Asia (Guo et al. 2019; Gao et al. 2020; Li et al. 2020; Yun et al. 2020), the European region (Kendon et al. 2012; Ban et al. 2014; Adinolfi et al. 2021), West Africa (Berthou et al. 2019), and the Andes region (Mourre et al. 2016; Moya-Álvarez et al. 2019; Junquas et al. 2022). However, in the United States, there is a general dry bias over the central and southeast plains and a positive precipitation bias over the Rockies during the boreal warm season (Sun et al. 2016; Liu et al. 2017; Gensini et al. 2023). In the meanwhile, the simulation results in this study are more sensitive to the PBL scheme than the MP and LSM schemes. This is similar to the results of Kouadio et al. (2020), which revealed a stronger impact of PBL than MP, with a better performance of the ACM2 non-local PBL scheme when simulating rainfall distribution over the Guinean coast and surroundings. Meroni et al. (2021) found the PBL scheme has a greater impact than MP on the structure and distribution of heavy rainfall on the African continent. Prein et al. (2022) also indicated mesoscale

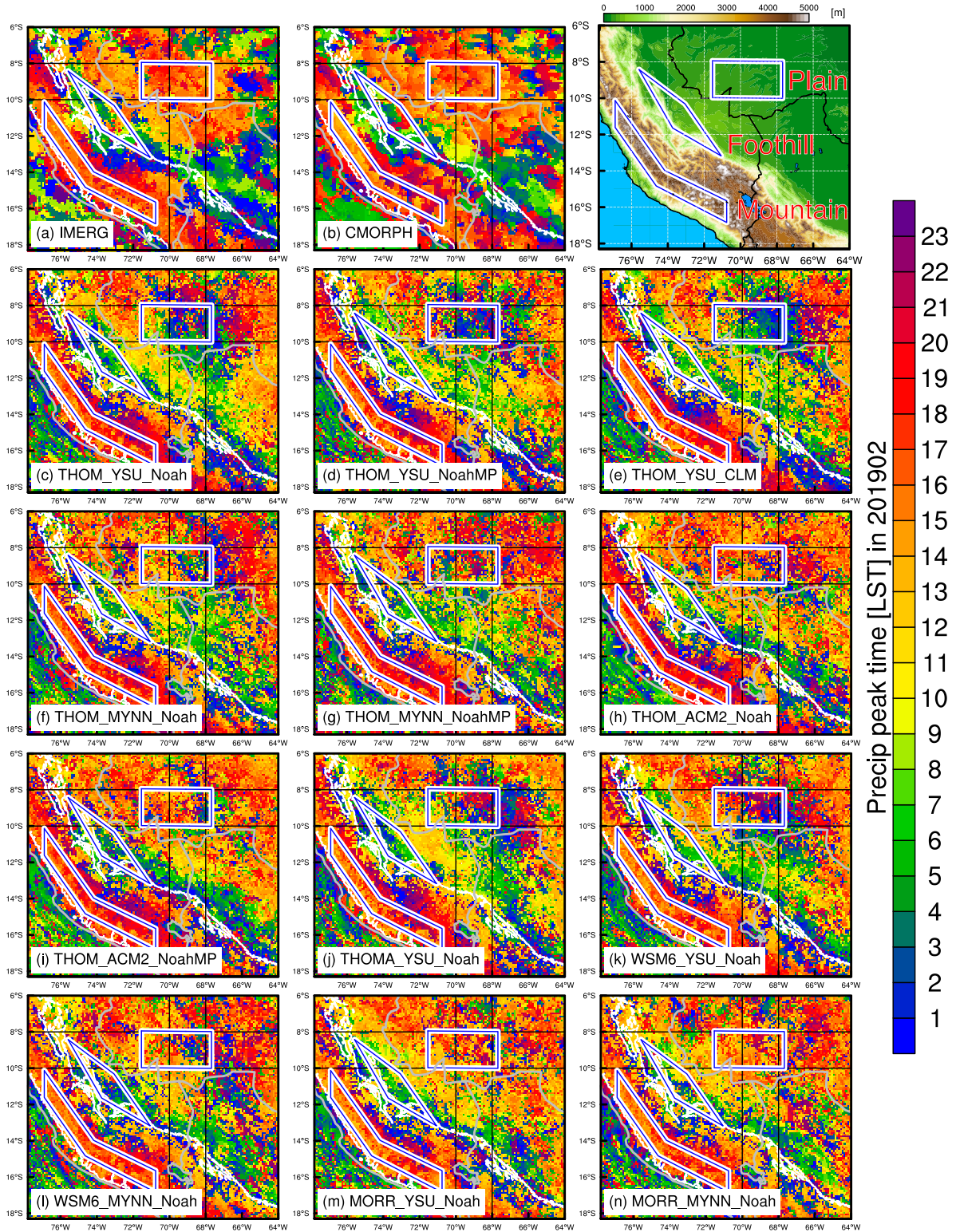


FIG. 5. Precipitation peak time (shaded; LST) calculated from (a) IMERG, (b) CMORPH, and (c)–(n) WRF simulations using different physics schemes in February 2019. The white contour in each panel represents 1-km terrain elevation. The blue polygons in each panel indicate the regions for diurnal precipitation calculation shown in Fig. 6, and terrain height in the study region is shown in the top-right panel. The black rectangles in each panel indicate the regions for Figs. 9 and 10.

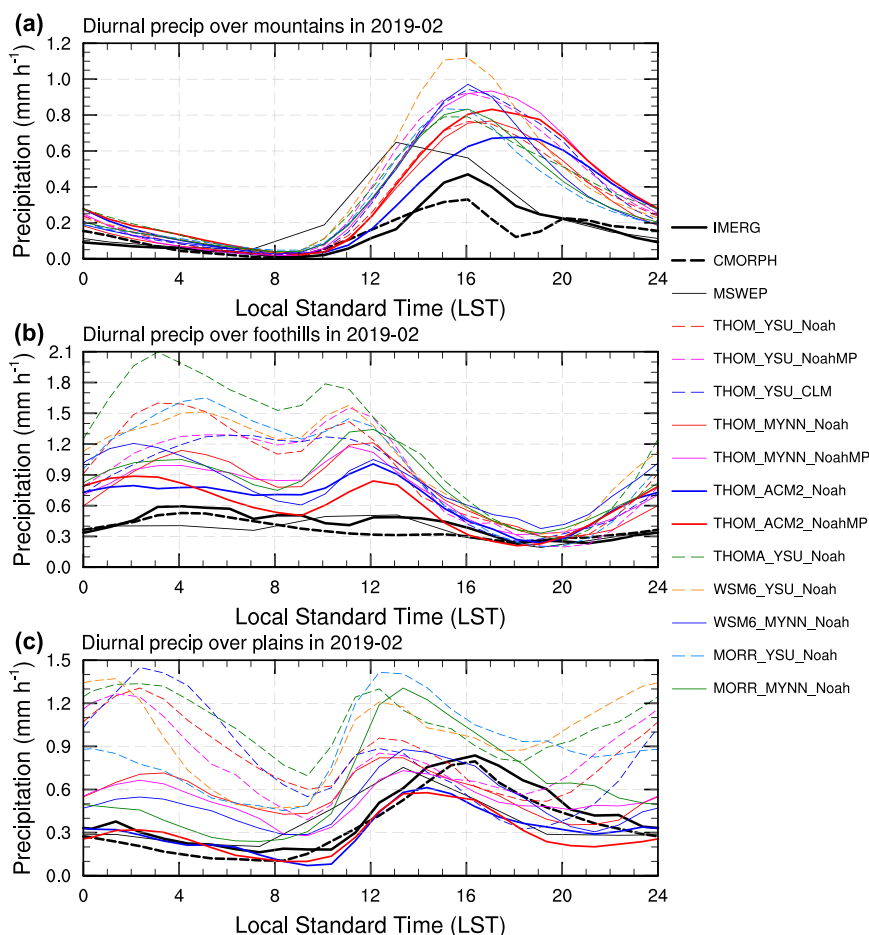


FIG. 6. Averaged diurnal precipitation ( $\text{mm h}^{-1}$ ) in the (a) mountain, (b) foothill, and (c) plains regions shown in Fig. 5 from IMERG, CMORPH, MSWEP (3-hourly mean), and WRF simulations using different physics schemes in February 2019.

convective systems in the central United States are more sensitive to MP, while PBL schemes are more influential in Brazil. Thus, differences among the simulations using different PBL schemes are further investigated in the next section.

### c. Differences in PBL schemes

To examine the differences in the simulations due to using different PBL schemes, three simulations, that is, THOM\_YSU\_Noah, THOM\_MYNN\_Noah, and THOM\_ACM2\_Noah, which differ only in the PBL scheme used, are selected for further analysis. Because the low-level wind field is crucial to moisture transport and convection triggering, mean wind vectors at 925 hPa from ERA5 and the difference between the three simulations and ERA5 in February 2019 are displayed in Figs. 8a(1)–d(1). From mean winds in Fig. 8a(1), northerly winds prevail at 925 hPa along the Andes. The prevailing northerly winds combined with the notches of terrain result in the four precipitation hotspots along the Andes (Fig. 2). The differences in mean winds between simulated and ERA5 winds [Figs. 8b(1)–d(1)] are smaller than  $1 \text{ m s}^{-1}$ , indicating the simulated mean winds in THOM\_YSU\_Noah,

THOM\_MYNN\_Noah, and THOM\_ACM2\_Noah are consistent with ERA5. Our preliminary tests (not shown) indicate that this is mainly associated with the spectral nudging used in the 15-km domain, which makes simulated large-scale circulations consistent with those of ERA5.

From the diurnal deviation wind vectors shown in Figs. 8a(2)–d(2), the simulations capture the evolution of deviation wind vectors well, which is consistent with ERA5, while the amplitudes of deviation winds are relatively large in the simulations, especially in THOM\_YSU\_Noah. The evolution of daily deviation winds can mostly be explained by the Blackadar inertial oscillation theory (Blackadar 1957), which is closely tied to boundary layer mixing and therefore influenced by the choice of PBL scheme. The critical roles of boundary layer inertial oscillations in producing nighttime/early morning precipitation in the rainy season in different regions have been demonstrated, such as in the Asian monsoon region (Xue et al. 2018; Zhang et al. 2019; Chen 2020), the Great Plains of the United States (Higgins et al. 1997; Trier et al. 2010), and east of the Andes (Saulo et al. 2000; Vernekar et al. 2003; Nicolini and Skabar 2011).

### Precip Hovmoller diagram in 201902

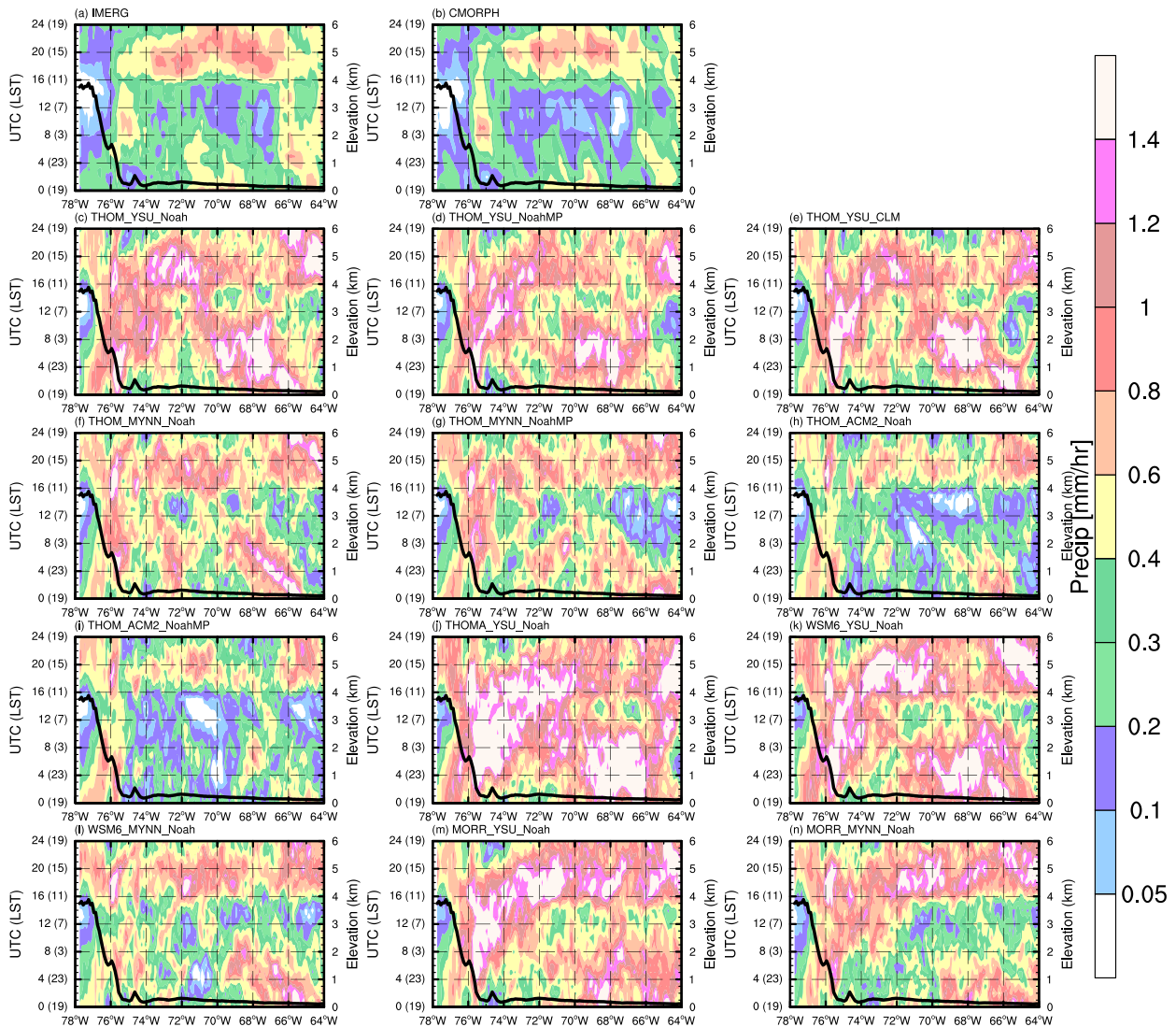


FIG. 7. Hovmöller diagrams of diurnal precipitation (shaded; mm h<sup>-1</sup>) for the region marked by the white rectangle shown in Fig. 2 from (a) IMERG, (b) CMORPH, and (c)–(n) WRF simulations using different physics schemes in February 2019. The black curve in each panel represents meridionally averaged terrain elevation (km) in the region marked by the white rectangle shown in Fig. 2. The left y axis is for the Hovmöller diagram and represents the time in UTC outside the parentheses and in the approximate LST (LST = UTC – 5 h, based on the longitude of 75°W) in the parentheses. The right y axis is for the terrain elevation.

From 1500 to 2100 UTC (1000–1600 LST), the deviation wind vectors have a large change in terms of direction and magnitude, especially over the western Amazon basin. The southerly deviation winds over the western Amazon basin at 2100 UTC (1600 LST) are in the opposite direction to the mean winds, which reduces the full winds. This is associated with daytime boundary layer mixing. The magnitudes of deviation winds at 2100 UTC (1600 LST) are the largest in THOM\_YSU\_Noah, followed by THOM\_MYNN\_Noah, and are the smallest in THOM\_ACM2\_Noah. The magnitudes of deviation winds in THOM\_ACM2\_Noah are closer to ERA5 than THOM\_YSU\_Noah and THOM\_MYNN\_Noah

[Figs. 8a(2)–d(2)]. It means that using different PBL schemes for simulations can lead to differences in boundary layer vertical mixing and then the evolution of large-scale wind fields, which influences the convergence of low-level winds in terms of both intensity and spatial distribution. From the 925-hPa wind divergence at 0300 UTC (2200 LST) [Figs. 8a(2)–d(2)], there are larger areas with wind convergence (divergence of less than  $-1 \times 10^{-5} \text{ s}^{-1}$ ) in THOM\_YSU\_Noah, which mainly covers the region of 10°–8°S, 70°–66°W, over the western Amazon basin. This can induce stronger and longer-lasting precipitation, which partially explains the stronger monthly and diurnal precipitation intensity and delayed precipitation



Cross sections of  $\theta_e$ ,  $Q_r$ , ( $u, w \times 20$ ) in 201902

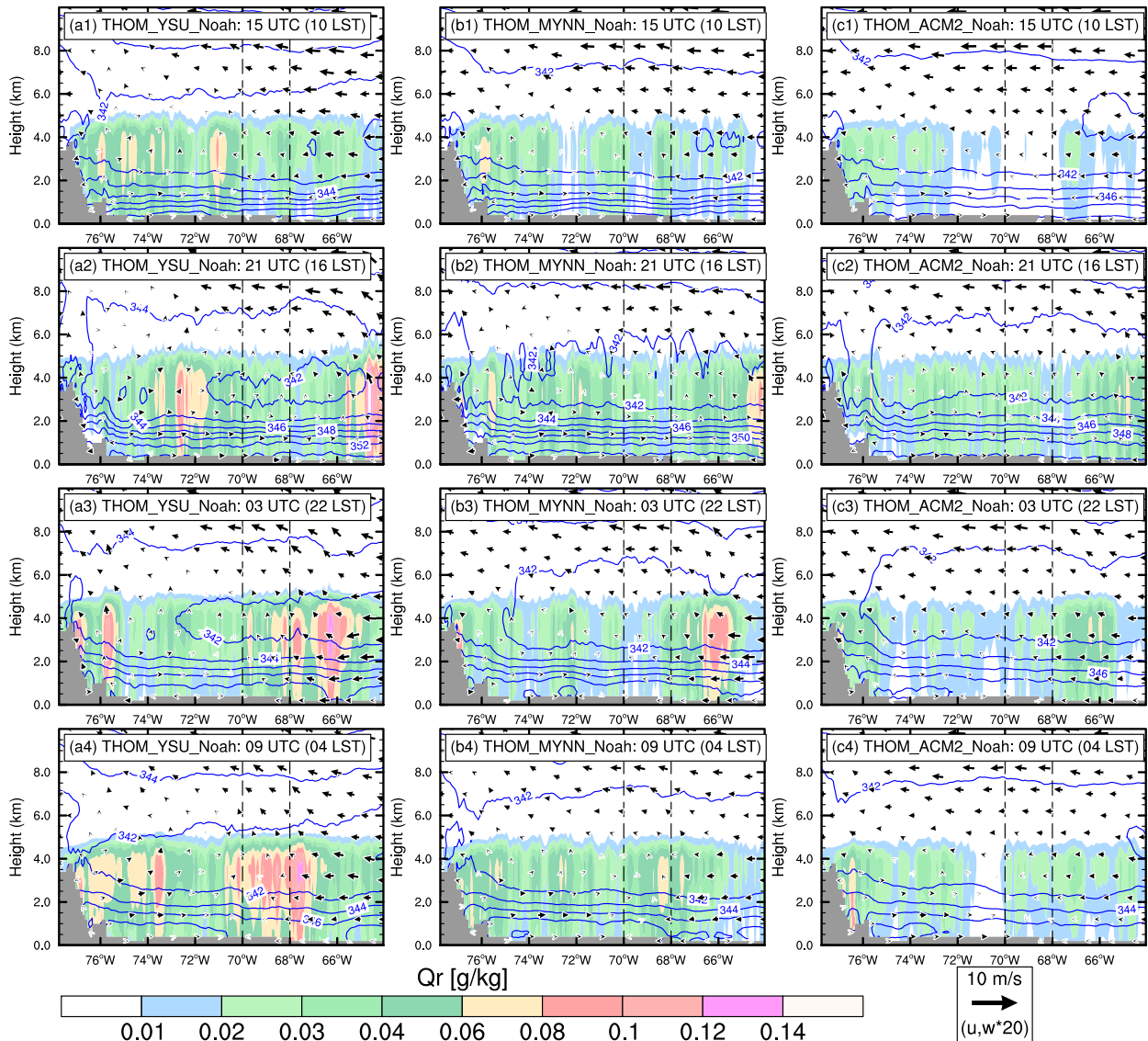


FIG. 9. Vertical cross sections of meridionally averaged equivalent potential temperature ( $\theta_e$ , K, blue contours in 2-K intervals), rainwater mixing ratio ( $Q_r$ ; shaded;  $\text{g kg}^{-1}$ ), and wind vectors ( $u, w \times 20$ ) for the region of  $10^\circ\text{--}8^\circ\text{S}$ ,  $78^\circ\text{--}64^\circ\text{W}$  shown in Fig. 5 at [a(1)]–[c(1)] 1500 UTC (1000 LST), [a(2)]–[c(2)] 2100 (1600 LST), [a(3)]–[c(3)] 0300 (2200 LST), and [a(4)]–[c(4)] 0900 UTC (0400 LST) in (left) THOM\_YSU\_Noah, (center) THOM\_MYNN\_Noah, and (right) THOM\_ACM2\_Noah in February 2019. The gray shaded area in each panel represents the missing value due to the terrain.

peak time over the western Amazon basin in THOM\_YSU\_Noah (as seen in Figs. 2, 5, and 7). This convergence is weaker in THOM\_MYNN\_Noah and THOM\_ACM2\_Noah [Figs. 8c(2),d(2)], which partially explains the weaker precipitation over the western Amazon basin during 0000–1200 UTC (1900–0700 LST) (Fig. 7).

To examine the differences in vertical dynamic and thermodynamic structures, the vertical cross sections of meridionally averaged and zonally averaged equivalent potential temperatures ( $\theta_e$ ), the rainwater mixing ratio ( $Q_r$ ), and wind vectors are shown in Figs. 9 and 10, respectively. At 1500 UTC

(1000 LST), the vertical gradient of  $\theta_e$  is larger in THOM\_YSU\_Noah and THOM\_MYNN\_Noah than in THOM\_ACM2\_Noah, where  $\theta_e$  increases from 344 to over 352 K from 2 km to the surface in THOM\_YSU\_Noah and THOM\_MYNN\_Noah, while it increases from 344 to  $\sim 350$  K in THOM\_ACM2\_Noah [Figs. 9a(1)–c(1), 10a(1)–c(1)]. Therefore, more warm, moist energy exists in the lower levels in THOM\_YSU\_Noah and THOM\_MYNN\_Noah than in THOM\_ACM2\_Noah. The horizontal winds in the upper levels are mainly easterly [Figs. 9a(1)–c(1)], while the horizontal winds in the lower levels are dominated by northerly winds [Figs. 10a(1)–c(1)].

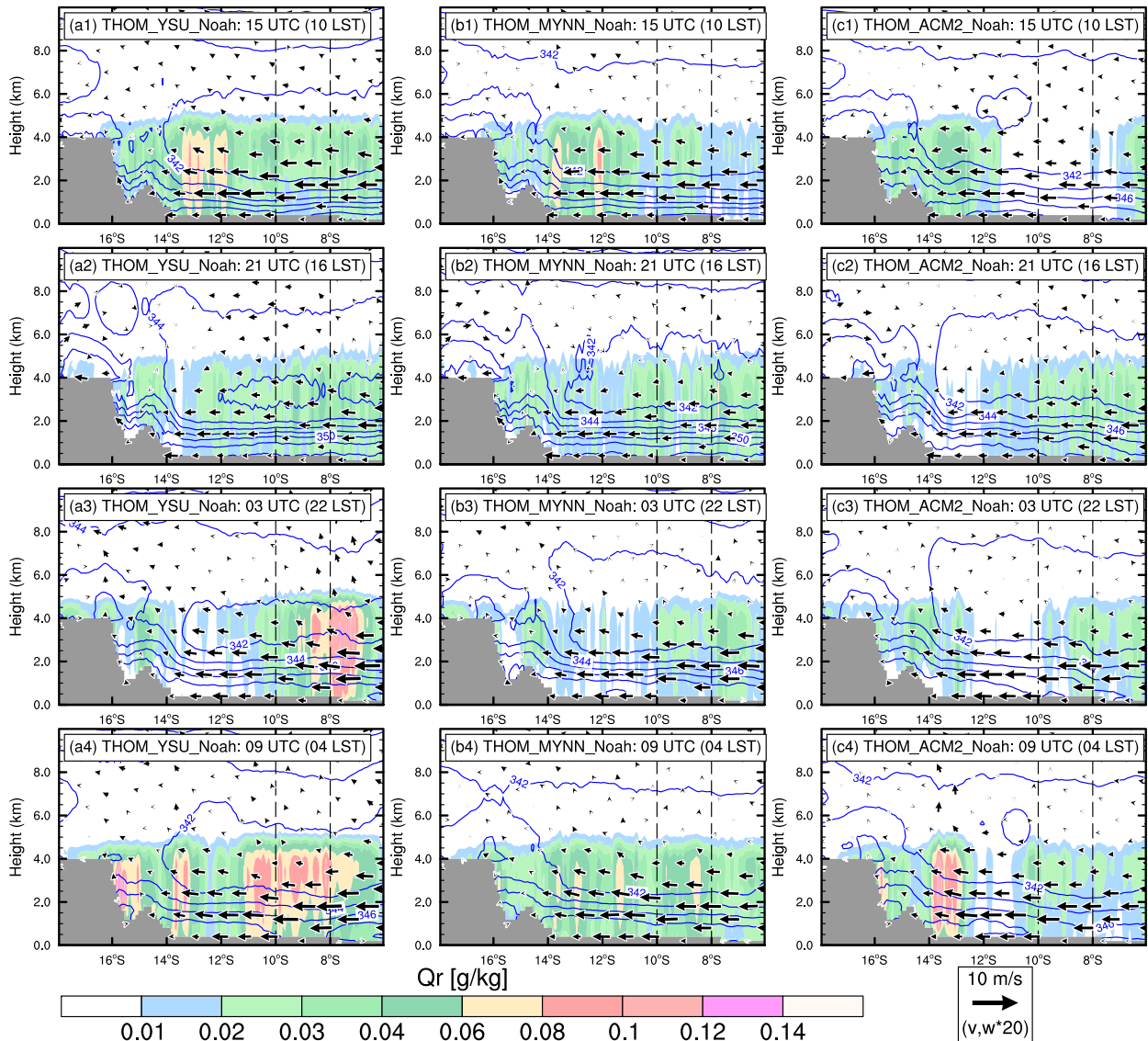
Cross sections of  $\theta_e$ ,  $Q_r$ , ( $v, w \times 20$ ) in 201902

FIG. 10. Vertical cross sections of zonally averaged equivalent potential temperature ( $\theta_e$ ; K; blue contours in 2-K intervals), rainwater mixing ratio ( $Q_r$ ; shaded;  $\text{g kg}^{-1}$ ), and wind vectors ( $v, w \times 20$ ) for the region of  $18^\circ\text{--}6^\circ\text{S}$ ,  $70^\circ\text{--}68^\circ\text{W}$  shown in Fig. 5 at [a(1)]–[c(1)] 1500 UTC (1000 LST), [a(2)]–[c(2)] 2100 UTC (1600 LST), [a(3)]–[c(3)] 0300 (22 LST), and [a(4)]–[c(4)] 0900 UTC (0400 LST) in (left) THOM\_YSU\_Noah, (center) THOM\_MYNN\_Noah, and (right) THOM\_ACM2\_Noah in February 2019. The gray shaded area in each panel represents the missing value due to the terrain.

The  $Q_r$  over the western Amazon basin is larger in THOM\_YSU\_Noah, where it can be over  $0.08 \text{ g kg}^{-1}$ , followed by THOM\_MYNN\_Noah, and least in THOM\_ACM2\_Noah [Figs. 9a(1)–c(1)], consistent with the differences in precipitation among the three simulations (Figs. 7c,f,h).

At 2100 UTC (1600 LST),  $\theta_e$  in the lower levels increases in all three simulations, to over 354 K near the surface in THOM\_YSU\_Noah and THOM\_MYNN\_Noah and to  $\sim 352$  K in THOM\_ACM2\_Noah [Figs. 9a(2)–c(2), 10a(2)–c(2)], which is mainly associated with solar radiative heating in the daytime. The low-level  $v$  winds weaken at 2100 UTC (1600 LST)

[Figs. 10a(2)–c(2)] compared to at 1500 UTC (1000 LST) [Figs. 10a(1)–c(1)], which is mainly associated with the daytime vertical mixing process (consistent with those shown in Fig. 8). The  $Q_r$  in THOM\_YSU\_Noah is larger than that in THOM\_MYNN\_Noah, resulting in stronger precipitation (Fig. 7c).

From 0300– to 0900 UTC (2200–0400 LST), there are more obvious convergences of  $u$  and  $v$  winds below 4 km and more warm, moist energy release in THOM\_YSU\_Noah [Figs. 9a(3),(4), 10a(3),(4), 8b(2)], associated with a faster decrease of  $\theta_e$ , especially in the region of  $10^\circ\text{--}8^\circ\text{S}$ ,  $70^\circ\text{--}66^\circ\text{W}$ .

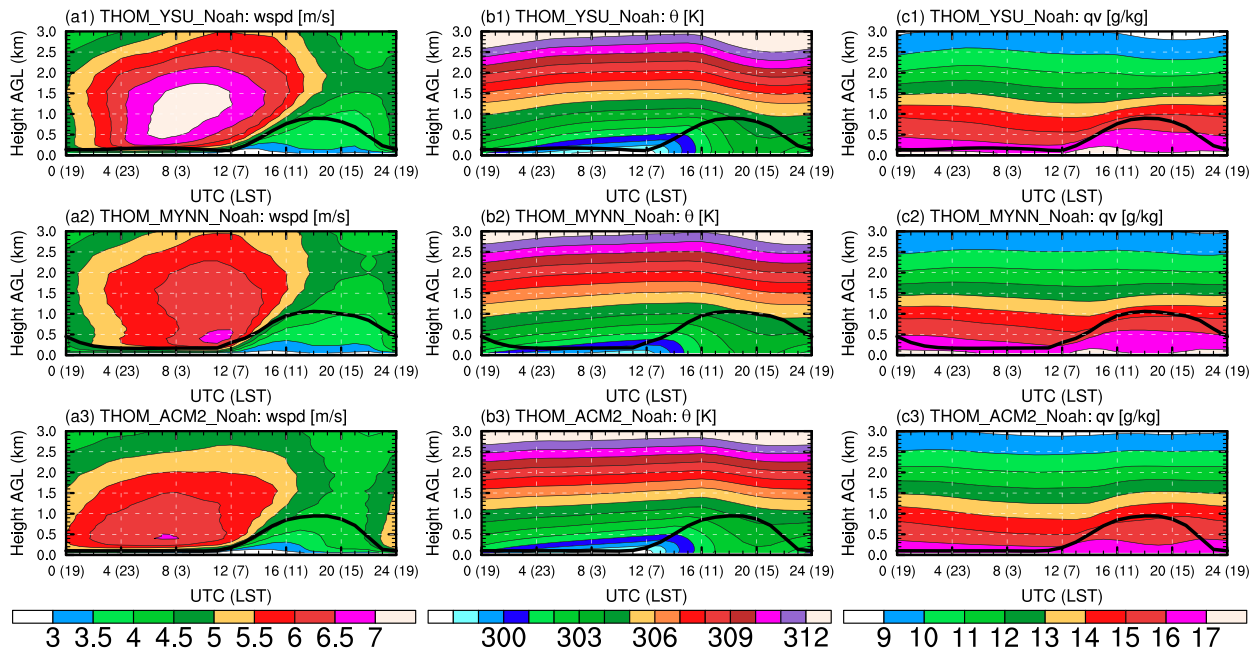


FIG. 11. Time–height sections of averaged [a(1)]–[a(3)] horizontal wspd ( $\text{m s}^{-1}$ ), [b(1)]–[b(3)] potential temperature ( $\theta$ ; K), and [c(1)]–[c(3)] specific humidity ( $q_v$ ;  $\text{g kg}^{-1}$ ) in the region of  $10^{\circ}$ – $8^{\circ}$ S,  $70^{\circ}$ – $68^{\circ}$ W in (top) THOM\_YSU\_Noah, (middle) THOM\_MYNN\_Noah, and (bottom) THOM\_ACM2\_Noah in February 2019. The black thick curves indicate averaged boundary layer height in each simulation. The x axis represents the time in UTC outside the parentheses and in LST (here, LST = UTC – 5 h in the examined region) in the parentheses. The y axis represents the height AGL (km) in each panel.

Thus,  $Q_r$  is larger and precipitation is stronger in THOM\_YSU\_Noah [Figs. 7c, 9a(3),(4), 10a(3),(4)]. The convergences of  $u$  and  $v$  winds below 4 km are weaker in THOM\_MYNN\_Noah [Figs. 9b(3),(4), 10b(3),(4), 8c(2)]. Although there is also high  $\theta_e$  in the low levels in THOM\_MYNN\_Noah, weaker wind convergence leads to less warm, moist energy release, resulting in less  $Q_r$  and weaker precipitation in THOM\_MYNN\_Noah [Figs. 7f, 9b(3),(4), 10b(3),(4)]. There are divergences of  $u$  and  $v$  winds below 4 km over the western Amazon basin, and  $\theta_e$  is generally lower in THOM\_ACM2\_Noah, leading to lesser  $Q_r$  and weaker precipitation [Figs. 7f, 8d(2), 9c(3),(4), 10c(3),(4)].

To further examine the differences in PBL structures in the three simulations, time–height sections of averaged horizontal wind speeds (wspd), potential temperature ( $\theta$ ), and specific humidity ( $q_v$ ) in the region of  $10^{\circ}$ – $8^{\circ}$ S,  $70^{\circ}$ – $68^{\circ}$ W in THOM\_YSU\_Noah, THOM\_MYNN\_Noah, and THOM\_ACM2\_Noah in February 2019 are displayed in Fig. 11. To see their evolution more clearly, differences in  $v$  winds, which dominate the horizontal winds (Figs. 8, 10),  $\theta$ , and  $q_v$  between current and previous hours are also plotted in Fig. 12 and represented as  $\Delta v$ ,  $\Delta \theta$ , and  $\Delta q_v$ , respectively. The evolution of  $\theta$  and  $q_v$  in the three simulations is similar in both daytime and nighttime [Figs. 11b(1)–(3),c(1)–(3)], while the vertical mixing of thermodynamics is stronger in THOM\_YSU\_Noah in the daytime, with  $\Delta \theta$  of over 0.4 K beyond the boundary layer top [Fig. 12b(1)]. The higher  $\theta$  and  $q_v$  in THOM\_YSU\_Noah and THOM\_MYNN\_Noah, where  $\theta$  and  $q_v$  are, respectively, more than 303 K and 17  $\text{g kg}^{-1}$  near the surface during

the daytime [Figs. 12b(1)–(3),c(1)–(3)], are consistent with the higher  $\theta_e$  in THOM\_YSU\_Noah and THOM\_MYNN\_Noah compared with THOM\_ACM2\_Noah [Figs. 9a(1)–c(2)].

There are larger differences in wspd evolution among the three simulations, especially in the nighttime [Figs. 11a(1)–(3)]. With the development of the boundary layer in the daytime (0600–1800 LST), wspd increases and its vertical gradient within the boundary layer in THOM\_YSU\_Noah (from less than  $3 \text{ m s}^{-1}$  near the surface to less than  $4 \text{ m s}^{-1}$  at the boundary layer top at 1600 LST) is smaller than those in THOM\_MYNN\_Noah (from less than  $3 \text{ m s}^{-1}$  near the surface to  $\sim 4 \text{ m s}^{-1}$  at the boundary layer top at 1600 LST) and THOM\_ACM2\_Noah (from less than  $3 \text{ m s}^{-1}$  near the surface to larger than  $4 \text{ m s}^{-1}$  at the boundary layer top at 1600 LST) [Figs. 11a(1)–(3)]. This is consistent with the larger  $\Delta v$  (over  $1 \text{ m s}^{-1}$ ) in THOM\_YSU\_Noah during 0700–1100 LST [Fig. 12a(1)], implying a stronger vertical mixing of momentum within the boundary layer. After 1500 LST, northerly winds start to develop below 3 km AGL in THOM\_ACM2\_Noah [Fig. 12a(3)], but it happens about 1 h later in THOM\_YSU\_Noah and 2 h later in THOM\_MYNN\_Noah (Figs. 12a(1),(2)). However, the development of northerly winds lasts longer in THOM\_YSU\_Noah, in which  $\Delta v < -0.2 \text{ m s}^{-1}$  and  $\Delta v < -0.4 \text{ m s}^{-1}$  can last to around 0300 LST and beyond 0000 LST, respectively, while  $\Delta v < -0.2 \text{ m s}^{-1}$  in THOM\_MYNN\_Noah and THOM\_ACM2\_Noah does not exist after 2300 LST [Figs. 12a(1)–(3)]. Therefore, a stronger low-level jet develops in THOM\_YSU\_Noah, with a maximum wspd over  $7 \text{ m s}^{-1}$  between 0.5 and 1.75 km AGL during the nighttime [Fig. 11a(1)],

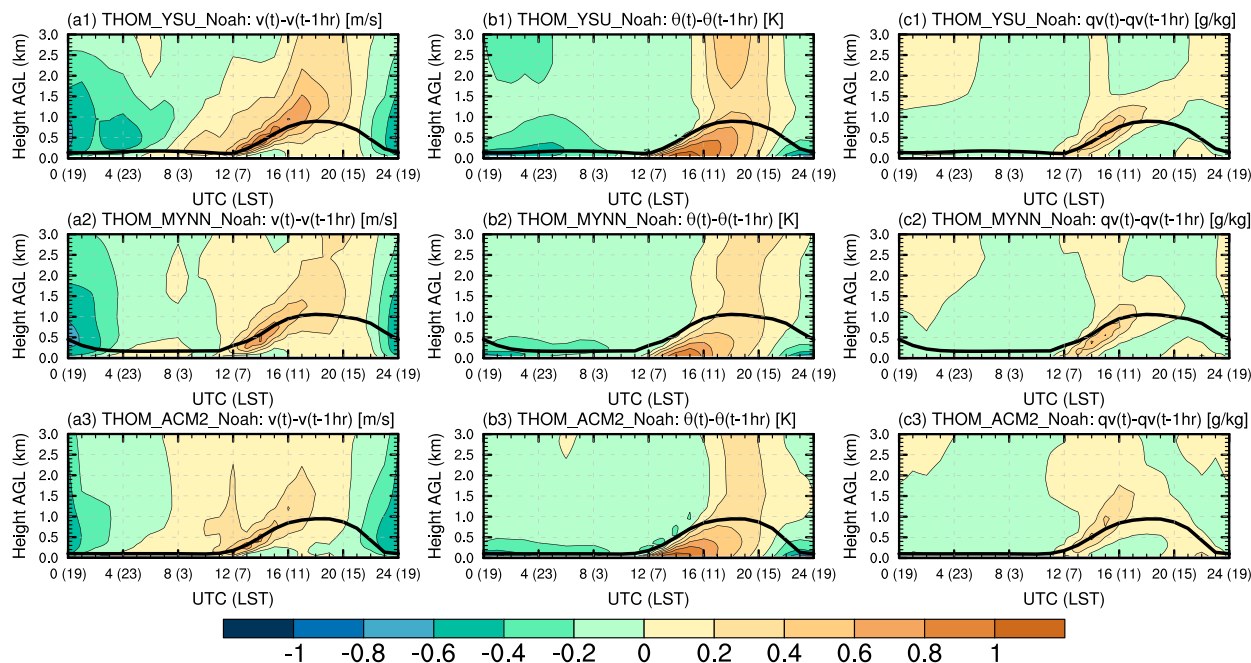


FIG. 12. As in Fig. 11, but for the differences in  $v$  winds, potential temperature ( $\theta$ ), and specific humidity ( $q_v$ ) between current hour and previous hour, referred to as [a(1)]–[a(3)]  $\Delta v$ , [b(1)]–[b(3)]  $\Delta \theta$ , and [c(1)]–[c(3)]  $\Delta q_v$ .

which is consistent with the stronger precipitation during 0400–0800 UTC (2300–0300 LST) in the examined region in THOM\_YSU\_Noah (Fig. 7c). The different precipitation peak time over the western Amazon basin among the three simulations (Figs. 5c,f,h) may be associated with the different developments of this low-level jet in the nighttime, which results from the different boundary layer mixing strength in the three PBL schemes. Martinez et al. (2022) also indicated that the choice of PBL scheme strongly impacts the development of low-level jets and subsequent precipitation in their 3-month simulations over the Colombian Andes region at a 12-km grid spacing. Martinez et al. (2022) also revealed that the simulation using the YSU scheme resulted in stronger low-level jets compared to the simulation using the MYNN scheme. These findings underscore the importance of selecting appropriate PBL schemes to improve precipitation simulation and forecasting in complex terrain regions.

The instantaneous time tendencies of  $v$  winds,  $\theta$ , and  $q_v$  due to PBL parameterization shown in Fig. 13 have similar patterns to the difference fields in Fig. 12 in the morning (0600–1200 LST), but different patterns appear after 1200 LST. It suggests that the accumulative effects of PBL parameterization start to influence the PBL processes in the afternoon. PBL parameterizations influence momentum, heat, moisture, and cloud fields, and there are also complex interactions among these fields. Differences in the strength of daytime boundary layer mixing and nighttime decay would affect the development of nocturnal low-level jets, transport of boundary layer moisture and momentum, low-level wind convergence, and final precipitation. The strength and distribution of precipitation would then have feedback to the low-level circulations, which

then again affect precipitation. Thus, it is difficult to link the accumulative effects to the tendencies due to PBL parameterization; in particular, the large-scale fields have been changed by the accumulative effects of PBL parameterization (Fig. 11). To examine the attribution of differences among the three simulations using different PBL schemes, especially the low-level jets in the nighttime, sensitivity experiments examining different terms (e.g., the local, nonlocal mixing, and boundary layer top entrainment terms) in the PBL schemes need to be performed. However, this aspect is outside the scope of this paper and has been thoroughly investigated in our subsequent publication (Hu et al. 2023), which indicated that the free-troposphere mixing in the presence of clouds appears to be the key factor in explaining the substantial difference in simulated precipitation between THOM\_YSU\_Noah and THOM\_ACM2\_Noah.

#### 4. Summary

To help choose the best physics configuration of a WRF-based regional climate model for performing dynamical downscaling of the future climate for the Peruvian central Andes region at a convection-permitting resolution, 12 two-month-long simulations using the WRF Model with different physics parameterization schemes are performed during January and February 2019 in the austral summer. The WRF Model is run with a 15-km grid covering all of South America, forced at the lateral boundaries by hourly ERA5 reanalysis data and a one-way nested 3-km grid covering the Peruvian central Andes region. The monthly and diurnal precipitation in the 3-km simulations is evaluated using rain gauge data in Peru and three higher-temporal-resolution global precipitation products, that is,

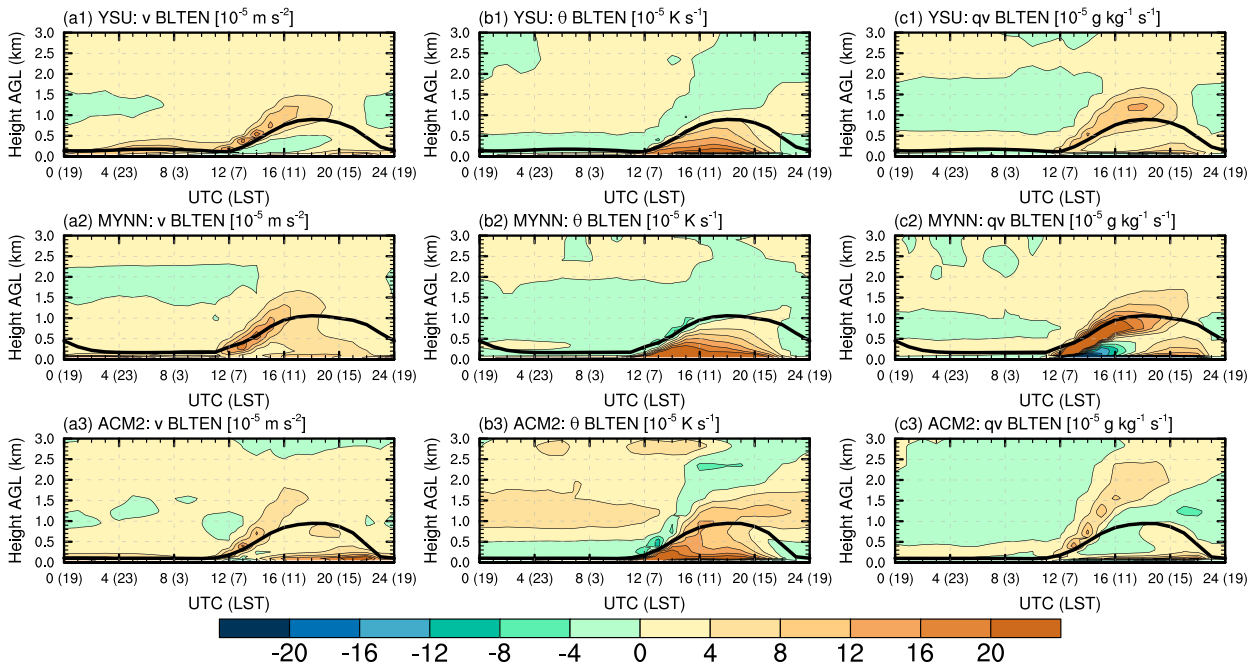


FIG. 13. Time–height sections of averaged instantaneous tendencies due to PBL parameterization of [a(1)]–[a(3)]  $v$  wind ( $10^{-5} \text{ m s}^{-2}$ ), [b(1)]–[b(3)] potential temperature ( $10^{-5} \text{ K s}^{-1}$ ), and [c(1)]–[c(3)] specific humidity ( $10^{-5} \text{ g kg}^{-1} \text{ s}^{-1}$ ) in the region of  $10^{\circ}$ – $8^{\circ}\text{S}$ ,  $70^{\circ}$ – $68^{\circ}\text{W}$  in (top) THOM\_YSU\_Noah, (middle) THOM\_MYNN\_Noah, and (bottom) THOM\_ACM2\_Noah in February 2019. The black thick curves indicate averaged boundary layer height in each simulation. The  $x$  axis represents the time in UTC outside the parentheses and in LST (here, LST = UTC – 5 h in the examined region) in the parentheses. The  $y$  axis represents the height AGL (km) in each panel.

IMERG, CMORPH, and MSWEP. The major results are summarized as follows:

- 1) Through comparing the monthly precipitation of the three global precipitation datasets and simulations to the rain gauge data, MSWEP shows the smallest RMSE, with a positive bias, and IMERG and CMORPH generally underestimate the monthly precipitation. All 12 simulations generally overestimate the precipitation, where the simulation using the Thompson microphysics scheme, ACM2 PBL scheme, and Noah land surface model has the smallest mean bias and RMSE, and the simulation using the Thompson aerosol-aware scheme, YSU PBL scheme, and Noah land surface model has the largest mean bias and RMSE.
- 2) All simulations successfully capture the four precipitation hotspots associated with the prevailing winds and terrain features along the east slope of the Peruvian central Andes. The simulated precipitation is the most sensitive to the PBL scheme, followed by the microphysics scheme, and is least sensitive to the LSM scheme. The simulated precipitation is generally stronger in the simulations using the YSU PBL scheme rather than the MYNN and ACM2 schemes. The simulation using the Thompson scheme, ACM2 PBL scheme, and Noah land surface model is the closest to the precipitation of IMERG and MSWEP.
- 3) Based on IMERG and CMORPH, the diurnal precipitation peak time is mainly in the afternoon ( $\sim 1400$ – $1900$  LST) over the Peruvian central Andes for terrain elevations higher

than 1 km, in the early morning ( $\sim 0000$ – $0600$  LST) along the east slope of the Peruvian central Andes for terrain elevations around 1 km, and between  $\sim 1400$  and  $1900$  LST over the western Amazon basin to the east of the Peruvian central Andes. All simulations successfully capture the precipitation peak time over the Peruvian central Andes and also along the east slope, while large differences exist in the precipitation peak time over the western Amazon basin, with about a 4–8-h delay in simulations using the YSU PBL scheme. The simulations using the ACM2 PBL scheme have a shorter delay.

- 4) Different PBL schemes can lead to differences in the evolution of large-scale low-level wind fields, which influences the intensity and spatial distribution of low-level wind convergence.  $\theta_e$  within the PBL is generally higher during the daytime in simulations using the YSU and MYNN schemes than in simulations using the ACM2 scheme, which is consistent with the stronger precipitation in simulations using the YSU and MYNN schemes. Obvious differences exist in the development of low-level jets during nighttime due to the accumulative effects of different PBL schemes. The stronger and longer-lasting low-level jets in simulations using the YSU scheme are consistent with the delayed precipitation peak time over the western Amazon basin.

These results provide guidance on the optimal configuration of regional climate models for future climate dynamical downscaling for the Peruvian central Andes region. Based on

the testing results, the YSU PBL scheme produces the highest bias in simulated precipitation as well as the longest delay in diurnal precipitation peak time. The ACM2 PBL scheme appears to be the preferred choice, while the MYNN PBL scheme also performs reasonably well. However, simulations over longer periods and spanning multiple years should be performed to make sure that such relative performances carry on to regional climate simulation application. We are currently running two configurations using the Thompson microphysics and Noah LSM schemes combined with the ACM2 and MYNN PBL schemes, respectively, and the results will be reported in the future. The configuration with better performance will be used for future convection-permitting regional climate simulations for the Peruvian central Andes region.

**Acknowledgments.** This project was primarily supported by Grant 20163646499 from the Universidad Nacional de San Agustín de Arequipa (UNSA) of Peru through the IREES/LASI Global Change and Human Health Institute. Supplementary funding was provided by the Weathernews Chair funds. The authors acknowledge the Texas Advanced Computing Center (TACC) at the University of Texas at Austin (<http://www.tacc.utexas.edu>) for providing HPC resources through XSEDE Allocation TG-ATM160014, which are used for the simulations. The authors also acknowledge high-performance computing support from Cheyenne (<https://doi.org/10.5065/D6RX99HX>), provided by NCAR's Computational and Information Systems Laboratory. NCAR is sponsored by the National Science Foundation. Some data processing was performed at the University of Oklahoma (OU) Supercomputing Center for Education and Research (OSCER).

**Data availability statement.** ERA5 reanalysis data are available at <https://doi.org/10.5065/BH6N-5N20>. The GPM IMERG final precipitation dataset is available at <https://doi.org/10.5067/GPM/IMERGDF/DAY/06> (last accessed 12 November 2020). The CMORPH dataset is available at [https://ftp.cpc.ncep.noaa.gov/precip/CMORPH\\_V1.0/CRT/8km-30min](https://ftp.cpc.ncep.noaa.gov/precip/CMORPH_V1.0/CRT/8km-30min) (last accessed 12 November 2020). The MSWEP dataset is available at <http://www.gloh2o.org/mswep> (last accessed 17 July 2021). The rain gauge data are available at <https://piscoprec.github.io/webPISCO/en/raingauges> (last accessed 18 July 2021). The model outputs are too large to be publicly archived. Please contact the corresponding author for more information.

## REFERENCES

- Adinolfi, M., M. Raffa, A. Reder, and P. Mercogliano, 2021: Evaluation and expected changes of summer precipitation at convection permitting scale with COSMO-CLM over Alpine space. *Atmosphere*, **12**, 54, <https://doi.org/10.3390/atmos12010054>.
- Ambrizzi, T., M. S. Reboita, R. P. da Rocha, and M. Llopert, 2019: The state of the art and fundamental aspects of regional climate modeling in South America. *Ann. N. Y. Acad. Sci.*, **1436**, 98–120, <https://doi.org/10.1111/nyas.13932>.
- Avila-Diaz, A., G. Abrahão, F. Justino, R. Torres, and A. Wilson, 2020: Extreme climate indices in Brazil: Evaluation of down-scaled Earth system models at high horizontal resolution. *Climate Dyn.*, **54**, 5065–5088, <https://doi.org/10.1007/s00382-020-05272-9>.
- Aybar, C., C. Fernández, A. Huerta, W. Lavado, F. Vega, and O. Felipe-Obando, 2020: Construction of a high-resolution gridded rainfall dataset for Peru from 1981 to the present day. *Hydrol. Sci. J.*, **65**, 770–785, <https://doi.org/10.1080/02626667.2019.1649411>.
- Ban, N., J. Schmidli, and C. Schär, 2014: Evaluation of the convection-resolving regional climate modeling approach in decade-long simulations. *J. Geophys. Res. Atmos.*, **119**, 7889–7907, <https://doi.org/10.1002/2014JD021478>.
- Beck, H. E., E. F. Wood, M. Pan, C. K. Fisher, D. G. Miralles, A. I. J. M. van Dijk, T. R. McVicar, and R. F. Adler, 2019: MSWEP V2 global 3-hourly 0.1° precipitation: Methodology and quantitative assessment. *Bull. Amer. Meteor. Soc.*, **100**, 473–500, <https://doi.org/10.1175/BAMS-D-17-0138.1>.
- Berthou, S., D. P. Rowell, E. J. Kendon, M. J. Roberts, R. A. Stratton, J. A. Crook, and C. Wilcox, 2019: Improved climatological precipitation characteristics over West Africa at convection-permitting scales. *Climate Dyn.*, **53**, 1991–2011, <https://doi.org/10.1007/s00382-019-04759-4>.
- , E. J. Kendon, S. C. Chan, N. Ban, D. Leutwyler, C. Schär, and G. Fosser, 2020: Pan-European climate at convection-permitting scale: A model intercomparison study. *Climate Dyn.*, **55**, 35–59, <https://doi.org/10.1007/s00382-018-4114-6>.
- Bettolli, M. L., and Coauthors, 2021: The CORDEX flagship pilot study in southeastern South America: A comparative study of statistical and dynamical downscaling models in simulating daily extreme precipitation events. *Climate Dyn.*, **56**, 1589–1608, <https://doi.org/10.1007/s00382-020-05549-z>.
- Blackadar, A. K., 1957: Boundary layer wind maxima and their significance for the growth of nocturnal inversions. *Bull. Amer. Meteor. Soc.*, **38**, 283–290, <https://doi.org/10.1175/1520-0477-38.5.283>.
- Chan, S. C., E. J. Kendon, S. Berthou, G. Fosser, E. Lewis, and H. J. Fowler, 2020: Europe-wide precipitation projections at convection permitting scale with the Unified Model. *Climate Dyn.*, **55**, 409–428, <https://doi.org/10.1007/s00382-020-05192-8>.
- Chavez, S. P., and K. Takahashi, 2017: Orographic rainfall hot spots in the Andes–Amazon transition according to the TRMM precipitation radar and in situ data. *J. Geophys. Res. Atmos.*, **122**, 5870–5882, <https://doi.org/10.1002/2016JD026282>.
- , Y. Silva, and A. P. Barros, 2020: High-elevation monsoon precipitation processes in the central Andes of Peru. *J. Geophys. Res. Atmos.*, **125**, e2020JD032947, <https://doi.org/10.1029/2020JD032947>.
- Chen, G., 2020: Diurnal cycle of the Asian summer monsoon: Air pump of the second kind. *J. Climate*, **33**, 1747–1775, <https://doi.org/10.1175/JCLI-D-19-0210.1>.
- Chen, M., and Coauthors, 2022: Cross-examining precipitation products by rain gauge, remote sensing, and WRF simulations over a South American region across the Pacific coast and Andes. *Atmosphere*, **13**, 1666, <https://doi.org/10.3390/atmos13101666>.
- Chimborazo, O., and M. Vuille, 2021: Present-day climate and projected future temperature and precipitation changes in Ecuador. *Theor. Appl. Climatol.*, **143**, 1581–1597, <https://doi.org/10.1007/s00704-020-03483-y>.
- Ciarlo, J. M., and Coauthors, 2020: A new spatially distributed added value index for regional climate models: The EURO-CORDEX

- and the CORDEX-CORE highest resolution ensembles. *Climate Dyn.*, **57**, 1403–1424, <https://doi.org/10.1007/s00382-020-05400-5>.
- Coppola, E., and Coauthors, 2020: A first-of-its-kind multi-model convection permitting ensemble for investigating convective phenomena over Europe and the Mediterranean. *Climate Dyn.*, **55**, 3–34, <https://doi.org/10.1007/s00382-018-4521-8>.
- da Silva, M. L., C. P. de Oliveira, C. M. Santos e Silva, and J. M. de Araújo, 2023: Dynamic downscaling of climate simulations and projected changes in tropical South America using RegCM4.7. *Int. J. Climatol.*, **43**, 3391–3415, <https://doi.org/10.1002/joc.8035>.
- de Sousa Afonso, J. M., D. A. Vila, M. A. Gan, D. P. Quispe, N. de Jesus da Costa Barreto, J. H. Huamán Chinchay, and R. S. A. Palharini, 2020: Precipitation diurnal cycle assessment of satellite-based estimates over Brazil. *Remote Sens.*, **12**, 2339, <https://doi.org/10.3390/rs12142339>.
- Dezfuli, A. K., C. M. Ichoku, G. J. Huffman, K. I. Mohr, J. S. Selker, N. van de Giesen, R. Hochreutener, and F. O. Annor, 2017: Validation of IMERG precipitation in Africa. *J. Hydrometeorol.*, **18**, 2817–2825, <https://doi.org/10.1175/JHM-D-17-0139.1>.
- Ek, M. B., K. E. Mitchell, Y. Lin, E. Rogers, P. Grunmann, V. Koren, G. Gayno, and J. D. Tarpley, 2003: Implementation of Noah land surface model advances in the National Centers for Environmental Prediction operational mesoscale Eta Model. *J. Geophys. Res.*, **108**, 8851, <https://doi.org/10.1029/2002JD003296>.
- Espinoza, J. C., S. Chavez, J. Ronchail, C. Junquas, K. Takahashi, and W. Lavado, 2015: Rainfall hotspots over the southern tropical Andes: Spatial distribution, rainfall intensity, and relations with large-scale atmospheric circulation. *Water Resour. Res.*, **51**, 3459–3475, <https://doi.org/10.1002/2014WR016273>.
- Falco, M., A. F. Carril, L. Z. X. Li, C. Cabrelli, and C. G. Menéndez, 2020: The potential added value of regional climate models in South America using a multiresolution approach. *Climate Dyn.*, **54**, 1553–1569, <https://doi.org/10.1007/s00382-019-05073-9>.
- Feng, Z., L. R. Leung, R. A. Houze Jr., S. Hagos, J. Hardin, Q. Yang, B. Han, and J. Fan, 2018: Structure and evolution of mesoscale convective systems: Sensitivity to cloud microphysics in convection-permitting simulations over the United States. *J. Adv. Model. Earth Syst.*, **10**, 1470–1494, <https://doi.org/10.1029/2018MS001305>.
- Feser, F., B. Rockel, H. von Storch, J. Winterfeldt, and M. Zahn, 2011: Regional climate models add value to global model data: A review and selected examples. *Bull. Amer. Meteor. Soc.*, **92**, 1181–1192, <https://doi.org/10.1175/2011BAMS3061.1>.
- Fosser, G., S. Khodayar, and P. Berg, 2015: Benefit of convection permitting climate model simulations in the representation of convective precipitation. *Climate Dyn.*, **44**, 45–60, <https://doi.org/10.1007/s00382-014-2242-1>.
- , E. J. Kendon, D. Stephenson, and S. Tucker, 2020: Convection-permitting models offer promise of more certain extreme rainfall projections. *Geophys. Res. Lett.*, **47**, e2020GL088151, <https://doi.org/10.1029/2020GL088151>.
- Fumière, Q., M. Déqué, O. Nuissier, S. Somot, A. Alias, C. Caillaud, O. Laurantin, and Y. Seity, 2020: Extreme rainfall in Mediterranean France during the fall: Added value of the CNRM-AROME convection-permitting regional climate model. *Climate Dyn.*, **55**, 77–91, <https://doi.org/10.1007/s00382-019-04898-8>.
- Gao, X., Y. Xu, Z. Zhao, J. S. Pal, and F. Giorgi, 2006: On the role of resolution and topography in the simulation of East Asia precipitation. *Theor. Appl. Climatol.*, **86**, 173–185, <https://doi.org/10.1007/s00704-005-0214-4>.
- Gao, Y., L. R. Leung, C. Zhao, and S. Hagos, 2017: Sensitivity of U.S. summer precipitation to model resolution and convective parameterizations across gray zone resolutions. *J. Geophys. Res. Atmos.*, **122**, 2714–2733, <https://doi.org/10.1002/2016JD025896>.
- , F. Chen, and Y. Jiang, 2020: Evaluation of a convection-permitting modeling of precipitation over the Tibetan Plateau and its influences on the simulation of snow-cover fraction. *J. Hydrometeorol.*, **21**, 1531–1548, <https://doi.org/10.1175/JHM-D-19-0277.1>.
- Gensini, V. A., A. M. Haberlie, and W. S. Ashley, 2023: Convection-permitting simulations of historical and possible future climate over the contiguous United States. *Climate Dyn.*, **60**, 109–126, <https://doi.org/10.1007/s00382-022-06306-0>.
- Giorgi, F., 2006: Regional climate modeling: Status and perspectives. *J. Phys. IV*, **139**, 101–118, <https://doi.org/10.1051/jp4:2006139008>.
- , 2019: Thirty years of regional climate modeling: Where are we and where are we going next? *J. Geophys. Res. Atmos.*, **124**, 5696–5723, <https://doi.org/10.1029/2018JD030094>.
- , and G. T. Bates, 1989: The climatological skill of a regional model over complex terrain. *Mon. Wea. Rev.*, **117**, 2325–2347, [https://doi.org/10.1175/1520-0493\(1989\)117<2325:TCSOAR>2.0.CO;2](https://doi.org/10.1175/1520-0493(1989)117<2325:TCSOAR>2.0.CO;2).
- González-Rojí, S. J., M. Messmer, C. C. Raible, and T. F. Stocker, 2022: Sensitivity of precipitation in the highlands and lowlands of Peru to physics parameterization options in WRFV3.8.1. *Geosci. Model Dev.*, **15**, 2859–2879, <https://doi.org/10.5194/gmd-15-2859-2022>.
- Guo, Z., J. Fang, X. Sun, Y. Yang, and J. Tang, 2019: Sensitivity of summer precipitation simulation to microphysics parameterization over eastern China: Convection-permitting regional climate simulation. *J. Geophys. Res. Atmos.*, **124**, 9183–9204, <https://doi.org/10.1029/2019JD030295>.
- , —, —, J. Tang, Y. Yang, and J. Tang, 2020: Decadal long convection-permitting regional climate simulations over eastern China: Evaluation of diurnal cycle of precipitation. *Climate Dyn.*, **54**, 1329–1349, <https://doi.org/10.1007/s00382-019-05061-z>.
- Gutowski, W. J., Jr., and Coauthors, 2016: WCRP Coordinated Regional Downscaling Experiment (CORDEX): A diagnostic MIP for CMIP6. *Geosci. Model Dev.*, **9**, 4087–4095, <https://doi.org/10.5194/gmd-9-4087-2016>.
- He, C., F. Chen, M. Barlage, C. Liu, A. Newman, W. Tang, K. Ikeda, and R. Rasmussen, 2019: Can convection-permitting modeling provide decent precipitation for offline high-resolution snowpack simulations over mountains? *J. Geophys. Res. Atmos.*, **124**, 12 631–12 654, <https://doi.org/10.1029/2019JD030823>.
- Hersbach, H., and Coauthors, 2020: The ERA5 global reanalysis. *Quart. J. Roy. Meteor. Soc.*, **146**, 1999–2049, <https://doi.org/10.1002/qj.3803>.
- Higgins, R. W., Y. Yao, E. S. Yarosh, J. E. Janowiak, and K. C. Mo, 1997: Influence of the Great Plains low-level jet on summertime precipitation and moisture transport over the central United States. *J. Climate*, **10**, 481–507, [https://doi.org/10.1175/1520-0442\(1997\)010<0481:IOTGPL>2.0.CO;2](https://doi.org/10.1175/1520-0442(1997)010<0481:IOTGPL>2.0.CO;2).
- Hodnebrog, Ø., B. M. Steensen, L. Marelle, K. Alterskjaer, S. B. Dalsøren, and G. Myhre, 2022: Understanding model diversity in future precipitation projections for South America.

- Climate Dyn.*, **58**, 1329–1347, <https://doi.org/10.1007/s00382-021-05964-w>.
- Hong, S.-Y., and J.-O. J. Lim, 2006: The WRF single-moment 6-class microphysics scheme (WSM6). *Asia-Pac. J. Atmos. Sci.*, **42**, 129–151.
- Hu, X.-M., M. Xue, R. A. McPherson, E. Martin, D. H. Rosen-dahl, and L. Qiao, 2018: Precipitation dynamical downscal-ing over the Great Plains. *J. Adv. Model. Earth Syst.*, **10**, 421–447, <https://doi.org/10.1002/2017MS001154>.
- , and Coauthors, 2023: Effects of lower troposphere vertical mixing on simulated clouds and precipitation over the Ama- zon during the wet season. *J. Geophys. Res. Atmos.*, **128**, e2023JD038553, <https://doi.org/10.1029/2023JD038553>.
- Huang, Y., Y. Wang, L. Xue, X. Wei, L. Zhang, and H. Li, 2020: Comparison of three microphysics parameterization schemes in the WRF Model for an extreme rainfall event in the coastal metropolitan city of Guangzhou, China. *Atmos. Res.*, **240**, 104939, <https://doi.org/10.1016/j.atmosres.2020.104939>.
- Huffman, G., E. Stocker, D. Bolvin, E. Nelkin, and J. Tan, 2019: GPM IMERG final precipitation L3 1 day 0.1 degree  $\times$  0.1 degree, V06. Goddard Earth Sciences Data and Information Services Center, accessed 12 November 2020, <https://doi.org/10.5067/GPM/IMERGDF/DAY/06>.
- Iacono, M. J., J. S. Delamere, E. J. Mlawer, M. W. Shephard, S. A. Clough, and W. D. Collins, 2008: Radiative forcing by long-lived greenhouse gases: Calculations with the AER radi- ative transfer models. *J. Geophys. Res.*, **113**, D13103, <https://doi.org/10.1029/2008JD009944>.
- Jiménez, P. A., J. Dudhia, J. F. González-Rouco, J. Navarro, J. P. Montávez, and E. García-Bustamante, 2012: A revised scheme for the WRF surface layer formulation. *Mon. Wea. Rev.*, **140**, 898–918, <https://doi.org/10.1175/MWR-D-11-00056.1>.
- Jones, C., 2019: Recent changes in the South America low-level jet. *npj Climate Atmos. Sci.*, **2**, 20, <https://doi.org/10.1038/s41612-019-0077-5>.
- Joyce, R. J., J. E. Janowiak, P. A. Arkin, and P. Xie, 2004: CMORPH: A method that produces global precipitation esti- mates from passive microwave and infrared data at high spatial and temporal resolution. *J. Hydrometeor.*, **5**, 487–503, [https://doi.org/10.1175/1525-7541\(2004\)005<0487:CAMTPG>2.0.CO;2](https://doi.org/10.1175/1525-7541(2004)005<0487:CAMTPG>2.0.CO;2).
- Jukes, M., and Coauthors, 2020: The CMIP6 data request (DREQ, version 01.00. 31). *Geosci. Model Dev.*, **13**, 201–224, <https://doi.org/10.5194/gmd-13-201-2020>.
- Junquas, C., K. Takahashi, T. Condom, J.-C. Espinoza, S. Chávez, J.-E. Sicart, and T. Lebel, 2018: Understanding the influence of orography on the precipitation diurnal cycle and the asso- ciated atmospheric processes in the central Andes. *Climate Dyn.*, **50**, 3995–4017, <https://doi.org/10.1007/s00382-017-3858-8>.
- , and Coauthors, 2022: Regional climate modeling of the diurnal cycle of precipitation and associated atmospheric circulation patterns over an Andean glacier region (Antisana, Ecuador). *Climate Dyn.*, **58**, 3075–3104, <https://doi.org/10.1007/s00382-021-06079-y>.
- Kanamitsu, M., and H. Kanamaru, 2007: Fifty-seven-year Cali- fornia reanalysis downscaling at 10 km (CaRD10). Part I: System detail and validation with observations. *J. Climate*, **20**, 5553–5571, <https://doi.org/10.1175/2007JCLI1482.1>.
- Karki, R., S. ul Hasson, L. Gerlitz, U. Schickhoff, T. Scholten, and J. Böhrner, 2017: Quantifying the added value of convection- permitting climate simulations in complex terrain: A systematic evaluation of WRF over the Himalayas. *Earth Syst. Dyn.*, **8**, 507–528, <https://doi.org/10.5194/esd-8-507-2017>.
- Kendon, E. J., N. M. Roberts, C. A. Senior, and M. J. Roberts, 2012: Realism of rainfall in a very high-resolution regional climate model. *J. Climate*, **25**, 5791–5806, <https://doi.org/10.1175/JCLI-D-11-00562.1>.
- , R. A. Stratton, S. Tucker, J. H. Marsham, S. Berthou, D. P. Rowell, and C. A. Senior, 2019: Enhanced future changes in wet and dry extremes over Africa at convection-permitting scale. *Nat. Commun.*, **10**, 1794, <https://doi.org/10.1038/s41467-019-09776-9>.
- , A. Prein, C. Senior, and A. Stirling, 2021: Challenges and outlook for convection-permitting climate modelling. *Philos. Trans. Roy. Soc.*, **A379**, 20190547, <https://doi.org/10.1098/rsta.2019.0547>.
- Kouadio, K., S. Bastin, A. Konare, and V. O. Ajayi, 2020: Does convection-permitting simulate better rainfall distribution and extreme over Guinean coast and surroundings? *Climate Dyn.*, **55**, 153–174, <https://doi.org/10.1007/s00382-018-4308-y>.
- Lavin-Gullon, A., M. Feijóo, S. Solman, J. Fernández, R. P. da Rocha, and M. L. Bettolli, 2021: Synoptic forcing associated with extreme precipitation events over southeastern South America as depicted by a CORDEX FPS set of convection- permitting RCMs. *Climate Dyn.*, **56**, 3187–3203, <https://doi.org/10.1007/s00382-021-05637-8>.
- Lawrence, D. M., and Coauthors, 2011: Parameterization improve- ments and functional and structural advances in version 4 of the community land model. *J. Adv. Model. Earth Syst.*, **3**, M03001, <https://doi.org/10.1029/2011MS000045>.
- Leung, L. R., L. O. Mearns, F. Giorgi, and R. L. Wilby, 2003: Regional climate research: Needs and opportunities. *Bull. Amer. Meteor. Soc.*, **84**, 89–95.
- Li, P., K. Furtado, T. Zhou, H. Chen, J. Li, Z. Guo, and C. Xiao, 2020: The diurnal cycle of East Asian summer monsoon pre- cipitation simulated by the Met Office Unified Model at con- vection-permitting scales. *Climate Dyn.*, **55**, 131–151, <https://doi.org/10.1007/s00382-018-4368-z>.
- , —, —, —, and —, 2021: Convection-permitting modelling improves simulated precipitation over the central and eastern Tibetan Plateau. *Quart. J. Roy. Meteor. Soc.*, **147**, 341–362, <https://doi.org/10.1002/qj.3921>.
- Lind, P., and Coauthors, 2020: Benefits and added value of con- vection-permitting climate modeling over Fenno-Scandinavia. *Climate Dyn.*, **55**, 1893–1912, <https://doi.org/10.1007/s00382-020-05359-3>.
- Liu, C., and Coauthors, 2017: Continental-scale convection-per- mitting modeling of the current and future climate of North America. *Climate Dyn.*, **49**, 71–95, <https://doi.org/10.1007/s00382-016-3327-9>.
- Lucas-Picher, P., R. Laprise, and K. Winger, 2017: Evidence of added value in North American regional climate model hind- cast simulations using ever-increasing horizontal resolutions. *Climate Dyn.*, **48**, 2611–2633, <https://doi.org/10.1007/s00382-016-3227-z>.
- , D. Argüeso, E. Brisson, Y. Trambly, P. Berg, A. Lemonsu, S. Kotlarski, and C. Caillaud, 2021: Convection-permitting modeling with regional climate models: Latest developments and next steps. *Wiley Interdiscip. Rev.: Climate Change*, **12**, e731, <https://doi.org/10.1002/wcc.731>.
- Marengo, J. A., M. W. Douglas, and P. L. Silva Dias, 2002: The South American low-level jet east of the Andes during the 1999 LBA-TRMM and LBA-WET AMC campaign. *J. Geophys. Res.*, **107**, 8079, <https://doi.org/10.1029/2001JD001188>.
- , and Coauthors, 2010: Future change of climate in South America in the late twenty-first century: Intercomparison of

- scenarios from three regional climate models. *Climate Dyn.*, **35**, 1073–1097, <https://doi.org/10.1007/s00382-009-0721-6>.
- Martinez, J. A., P. A. Arias, C. Castro, H.-I. Chang, and C. A. Ochoa-Moya, 2019: Sea surface temperature–related response of precipitation in northern South America according to a WRF multi-decadal simulation. *Int. J. Climatol.*, **39**, 2136–2155, <https://doi.org/10.1002/joc.5940>.
- , —, C. Junquas, J. C. Espinoza, T. Condom, F. Dominguez, and J. S. Morales, 2022: The Orinoco low-level jet and the cross-equatorial moisture transport over tropical South America: Lessons from seasonal WRF simulations. *J. Geophys. Res. Atmos.*, **127**, e2021JD035603, <https://doi.org/10.1029/2021JD035603>.
- Meroni, A. N., K. A. Oundo, R. Muita, M.-J. Bopape, T. R. Maisha, M. Lagasio, A. Parodi, and G. Venuti, 2021: Sensitivity of some African heavy rainfall events to microphysics and planetary boundary layer schemes: Impacts on localised storms. *Quart. J. Roy. Meteor. Soc.*, **147**, 2448–2468, <https://doi.org/10.1002/qj.4033>.
- Miguez-Macho, G., G. L. Stenchikov, and A. Robock, 2004: Spectral nudging to eliminate the effects of domain position and geometry in regional climate model simulations. *J. Geophys. Res.*, **109**, D13104, <https://doi.org/10.1029/2003JD004495>.
- Mohr, K. I., D. Slayback, and K. Yager, 2014: Characteristics of precipitation features and annual rainfall during the TRMM era in the central Andes. *J. Climate*, **27**, 3982–4001, <https://doi.org/10.1175/JCLI-D-13-00592.1>.
- Montini, T. L., C. Jones, and L. M. V. Carvalho, 2019: The South American low-level jet: A new climatology, variability, and changes. *J. Geophys. Res. Atmos.*, **124**, 1200–1218, <https://doi.org/10.1029/2018JD029634>.
- Morrison, H., G. Thompson, and V. Tatarskii, 2009: Impact of cloud microphysics on the development of trailing stratiform precipitation in a simulated squall line: Comparison of one- and two-moment schemes. *Mon. Wea. Rev.*, **137**, 991–1007, <https://doi.org/10.1175/2008MWR2556.1>.
- Moufouma-Okia, W., and R. Jones, 2015: Resolution dependence in simulating the African hydroclimate with the HadGEM3-RA regional climate model. *Climate Dyn.*, **44**, 609–632, <https://doi.org/10.1007/s00382-014-2322-2>.
- Mourre, L., T. Condom, C. Junquas, T. Lebel, J. E. Sicart, R. Figueroa, and A. Cochachin, 2016: Spatio-temporal assessment of WRF, TRMM and in situ precipitation data in a tropical mountain environment (Cordillera Blanca, Peru). *Hydrol. Earth Syst. Sci.*, **20**, 125–141, <https://doi.org/10.5194/hess-20-125-2016>.
- Moya-Álvarez, A. S., D. Martínez-Castro, S. Kumar, R. Estevan, and Y. Silva, 2019: Response of the WRF Model to different resolutions in the rainfall forecast over the complex Peruvian orography. *Theor. Appl. Climatol.*, **137**, 2993–3007, <https://doi.org/10.1007/s00704-019-02782-3>.
- Nakanishi, M., and H. Niino, 2009: Development of an improved turbulence closure model for the atmospheric boundary layer. *J. Meteor. Soc. Japan*, **87**, 895–912, <https://doi.org/10.2151/jmsj.87.895>.
- Nicolini, M., and Y. G. Skabar, 2011: Diurnal cycle in convergence patterns in the boundary layer east of the Andes and convection. *Atmos. Res.*, **100**, 377–390, <https://doi.org/10.1016/j.atmosres.2010.09.019>.
- Niu, G.-Y., and Coauthors, 2011: The community Noah land surface model with multiparameterization options (Noah-MP): 1. Model description and evaluation with local-scale measurements. *J. Geophys. Res.*, **116**, D12109, <https://doi.org/10.1029/2010JD015139>.
- O, S., and P.-E. Kirstetter, 2018: Evaluation of diurnal variation of GPM IMERG–derived summer precipitation over the contiguous US using MRMS data. *Quart. J. Roy. Meteor. Soc.*, **144**, 270–281, <https://doi.org/10.1002/qj.3218>.
- Paccini, L., and B. Stevens, 2023: Assessing precipitation over the Amazon basin as simulated by a storm-resolving model. *J. Geophys. Res. Atmos.*, **128**, e2022JD037436, <https://doi.org/10.1029/2022JD037436>.
- Pleim, J. E., 2007: A combined local and nonlocal closure model for the atmospheric boundary layer. Part I: Model description and testing. *J. Appl. Meteor. Climatol.*, **46**, 1383–1395, <https://doi.org/10.1175/JAM2539.1>.
- Poveda, G., J. C. Espinoza, M. D. Zuluaga, S. A. Solman, R. Garreaud, and P. J. Van Oevelen, 2020: High impact weather events in the Andes. *Front. Earth Sci.*, **8**, 162, <https://doi.org/10.3389/feart.2020.00162>.
- Prein, A. F., A. Gobiet, M. Suklitsch, H. Truhetz, N. Awan, K. Keuler, and G. Georgievski, 2013: Added value of convection permitting seasonal simulations. *Climate Dyn.*, **41**, 2655–2677, <https://doi.org/10.1007/s00382-013-1744-6>.
- , and Coauthors, 2015: A review on regional convection-permitting climate modeling: Demonstrations, prospects, and challenges. *Rev. Geophys.*, **53**, 323–361, <https://doi.org/10.1002/2014RG000475>.
- , C. Liu, K. Ikeda, R. Bullock, R. M. Rasmussen, G. J. Holland, and M. Clark, 2020: Simulating North American mesoscale convective systems with a convection-permitting climate model. *Climate Dyn.*, **55**, 95–110, <https://doi.org/10.1007/s00382-017-3993-2>.
- , M. Ge, A. R. Valle, D. Wang, and S. E. Giangrande, 2022: Towards a unified setup to simulate mid-latitude and tropical mesoscale convective systems at kilometer-scales. *Earth Space Sci.*, **9**, e2022EA002295, <https://doi.org/10.1029/2022EA002295>.
- Rasmussen, K. L., and R. A. Houze Jr., 2016: Convective initiation near the Andes in subtropical South America. *Mon. Wea. Rev.*, **144**, 2351–2374, <https://doi.org/10.1175/MWR-D-15-0058.1>.
- Roads, J., and Coauthors, 2003: International Research Institute/Applied Research Centers (IRI/ARCs) regional model inter-comparison over South America. *J. Geophys. Res.*, **108**, 4425, <https://doi.org/10.1029/2002JD003201>.
- Romatschke, U., and R. A. Houze Jr., 2010: Extreme summer convection in South America. *J. Climate*, **23**, 3761–3791, <https://doi.org/10.1175/2010JCLI3465.1>.
- Rummukainen, M., 2016: Added value in regional climate modeling. *Wiley Interdiscip. Rev.: Climate Change*, **7**, 145–159, <https://doi.org/10.1002/wcc.378>.
- , B. Rockel, L. Bärring, J. H. Christensen, and M. Reckermann, 2015: Twenty-first-century challenges in regional climate modeling. *Bull. Amer. Meteor. Soc.*, **96**, ES135–ES138, <https://doi.org/10.1175/BAMS-D-14-00214.1>.
- Salio, P., M. Nicolini, and E. J. Zipser, 2007: Mesoscale convective systems over southeastern South America and their relationship with the South American low-level jet. *Mon. Wea. Rev.*, **135**, 1290–1309, <https://doi.org/10.1175/MWR3305.1>.
- Saulo, A. C., M. Nicolini, and S. C. Chou, 2000: Model characterization of the South American low-level flow during the 1997–1998 spring–summer season. *Climate Dyn.*, **16**, 867–881, <https://doi.org/10.1007/s003820000085>.
- Schumacher, V., A. Fernández, F. Justino, and A. Comin, 2020: WRF high resolution dynamical downscaling of precipitation

- for the central Andes of Chile and Argentina. *Front. Earth Sci.*, **8**, 328, <https://doi.org/10.3389/feart.2020.00328>.
- Skamarock, W. C., and Coauthors, 2019: A description of the Advanced Research WRF Model version 4. NCAR Tech. Note NCAR/TN-556+STR, 145 pp., <https://doi.org/10.5065/1dfh-6p97>.
- Solman, S. A., 2013: Regional climate modeling over South America: A review. *Adv. Meteor.*, **2013**, 504357, <https://doi.org/10.1155/2013/504357>.
- , and J. Blázquez, 2019: Multiscale precipitation variability over South America: Analysis of the added value of CORDEX RCM simulations. *Climate Dyn.*, **53**, 1547–1565, <https://doi.org/10.1007/s00382-019-04689-1>.
- Stratton, R. A., and Coauthors, 2018: A pan-African convection-permitting regional climate simulation with the Met Office Unified Model: CP4-Africa. *J. Climate*, **31**, 3485–3508, <https://doi.org/10.1175/JCLI-D-17-0503.1>.
- Sun, X., M. Xue, J. Brotzge, R. A. McPherson, X.-M. Hu, and X.-Q. Yang, 2016: An evaluation of dynamical downscaling of central plains summer precipitation using a WRF-based regional climate model at a convection-permitting 4 km resolution. *J. Geophys. Res. Atmos.*, **121**, 13 801–13 825, <https://doi.org/10.1002/2016JD024796>.
- Tan, J., G. J. Huffman, D. T. Bolvin, and E. J. Nelkin, 2019: Diurnal cycle of IMERG V06 precipitation. *Geophys. Res. Lett.*, **46**, 13 584–13 592, <https://doi.org/10.1029/2019GL085395>.
- Taraphdar, S., and Coauthors, 2021: WRF gray-zone simulations of precipitation over the Middle-East and the UAE: Impacts of physical parameterizations and resolution. *J. Geophys. Res. Atmos.*, **126**, e2021JD034648, <https://doi.org/10.1029/2021JD034648>.
- Taylor, K. E., 2001: Summarizing multiple aspects of model performance in a single diagram. *J. Geophys. Res.*, **106**, 7183–7192, <https://doi.org/10.1029/2000JD900719>.
- Thompson, G., and T. Eidhammer, 2014: A study of aerosol impacts on clouds and precipitation development in a large winter cyclone. *J. Atmos. Sci.*, **71**, 3636–3658, <https://doi.org/10.1175/JAS-D-13-0305.1>.
- , P. R. Field, R. M. Rasmussen, and W. D. Hall, 2008: Explicit forecasts of winter precipitation using an improved bulk microphysics scheme. Part II: Implementation of a new snow parameterization. *Mon. Wea. Rev.*, **136**, 5095–5115, <https://doi.org/10.1175/2008MWR2387.1>.
- Tiedtke, M., 1989: A comprehensive mass flux scheme for cumulus parameterization in large-scale models. *Mon. Wea. Rev.*, **117**, 1779–1800, [https://doi.org/10.1175/1520-0493\(1989\)117<1779:ACMFSF>2.0.CO;2](https://doi.org/10.1175/1520-0493(1989)117<1779:ACMFSF>2.0.CO;2).
- Torma, C., F. Giorgi, and E. Coppola, 2015: Added value of regional climate modeling over areas characterized by complex terrain—Precipitation over the Alps. *J. Geophys. Res. Atmos.*, **120**, 3957–3972, <https://doi.org/10.1002/2014JD022781>.
- Trier, S. B., C. Davis, and D. A. Ahijevych, 2010: Environmental controls on the simulated diurnal cycle of warm-season precipitation in the continental United States. *J. Atmos. Sci.*, **67**, 1066–1090, <https://doi.org/10.1175/2009JAS3247.1>.
- Vera, C., and Coauthors, 2006: The South American low-level jet experiment. *Bull. Amer. Meteor. Soc.*, **87**, 63–78, <https://doi.org/10.1175/BAMS-87-1-63>.
- Vernekar, A. D., B. P. Kirtman, and M. J. Fennessy, 2003: Low-level jets and their effects on the South American summer climate as simulated by the NCEP Eta Model. *J. Climate*, **16**, 297–311, [https://doi.org/10.1175/1520-0442\(2003\)016<0297:LLJATE>2.0.CO;2](https://doi.org/10.1175/1520-0442(2003)016<0297:LLJATE>2.0.CO;2).
- Watters, D., and A. Battaglia, 2019: The summertime diurnal cycle of precipitation derived from IMERG. *Remote Sens.*, **11**, 1781, <https://doi.org/10.3390/rs11151781>.
- Xue, M., X. Luo, K. Zhu, Z. Sun, and J. Fei, 2018: The controlling role of boundary layer inertial oscillations in meiyu frontal precipitation and its diurnal cycles over China. *J. Geophys. Res. Atmos.*, **123**, 5090–5115, <https://doi.org/10.1029/2018JD028368>.
- Yun, Y., C. Liu, Y. Luo, X. Liang, L. Huang, F. Chen, and R. Rasmussen, 2020: Convection-permitting regional climate simulation of warm-season precipitation over eastern China. *Climate Dyn.*, **54**, 1469–1489, <https://doi.org/10.1007/s00382-019-05070-y>.
- Zaninelli, P. G., C. G. Menéndez, M. Falco, N. López-Franca, and A. F. Carril, 2019: Future hydroclimatological changes in South America based on an ensemble of regional climate models. *Climate Dyn.*, **52**, 819–830, <https://doi.org/10.1007/s00382-018-4225-0>.
- Zhang, Y., M. Xue, K. Zhu, and B. Zhou, 2019: What is the main cause of diurnal variation and nocturnal peak of summer precipitation in Sichuan basin, China? The key role of boundary layer low-level jet inertial oscillations. *J. Geophys. Res. Atmos.*, **124**, 2643–2664, <https://doi.org/10.1029/2018JD029834>.
- Zhu, K., and M. Xue, 2016: Evaluation of WRF-based convection-permitting multi-physics ensemble forecasts over China for an extreme rainfall event on 21 July 2012 in Beijing. *Adv. Atmos. Sci.*, **33**, 1240–1258, <https://doi.org/10.1007/s00376-016-6202-z>.
- , and Coauthors, 2018: Evaluation of real-time convection-permitting precipitation forecasts in China during the 2013–2014 summer season. *J. Geophys. Res. Atmos.*, **123**, 1037–1064, <https://doi.org/10.1002/2017JD027445>.